



# Effects of geometric nonlinearities on the coupled dynamics of CNT strengthened composite beams with porosity, mass and geometric imperfections

Hossein B. Khaniki<sup>1</sup> · Mergen H. Ghayesh<sup>1</sup> · Shahid Hussain<sup>2</sup> · Marco Amabili<sup>3</sup>

Received: 21 February 2021 / Accepted: 3 July 2021 / Published online: 22 July 2021  
© The Author(s), under exclusive licence to Springer-Verlag London Ltd., part of Springer Nature 2021

## Abstract

This study investigates the effects of geometric nonlinearities on the dynamical behaviour of carbon nanotube (CNT) strengthened imperfect composite beams by considering both axial and transverse motions. For the given general model of the beam, the system modelling has been adopted from the literature and the nonlinear dynamic response in presence of an external harmonic load is examined for the first time in the case of axially functionally graded (AFG) CNT fibre, which is used for strengthening the structure. Porosity imperfection with the ability to vary through the thickness is modelled using simple, closed and open-cell models; the porosity variation is formulated using uniform, linear, symmetric and un-symmetric models. The geometrical imperfection is considered by allowing the beam to have an initial curved longitudinal axis and the mass imperfection is modelled by introducing a concentrated mass at a certain point of the beam. Using a combination of the Galerkin scheme together with dynamic equilibrium technique, the influence of different imperfections and porosities on the frequency response of the system is examined. It is shown that, for the case of AFG CNT strengthened beam, geometrical imperfection can change the nonlinear response from a hardening to a softening behaviour. Besides, the importance of considering the interaction between axial and transverse motion is examined in detail. The influence of lumped mass imperfection and its position is also studied showing that this type of imperfection can change the nonlinear behaviour of the system significantly. Moreover, the influence of increasing the CNT volume fraction and functionally spreading the CNTs through the length is discussed. The results are useful for analysing the resonance phenomena in strengthened structures facing various imperfections.

---

✉ Hossein B. Khaniki  
hossein.bakhshikhaniki@adelaide.edu

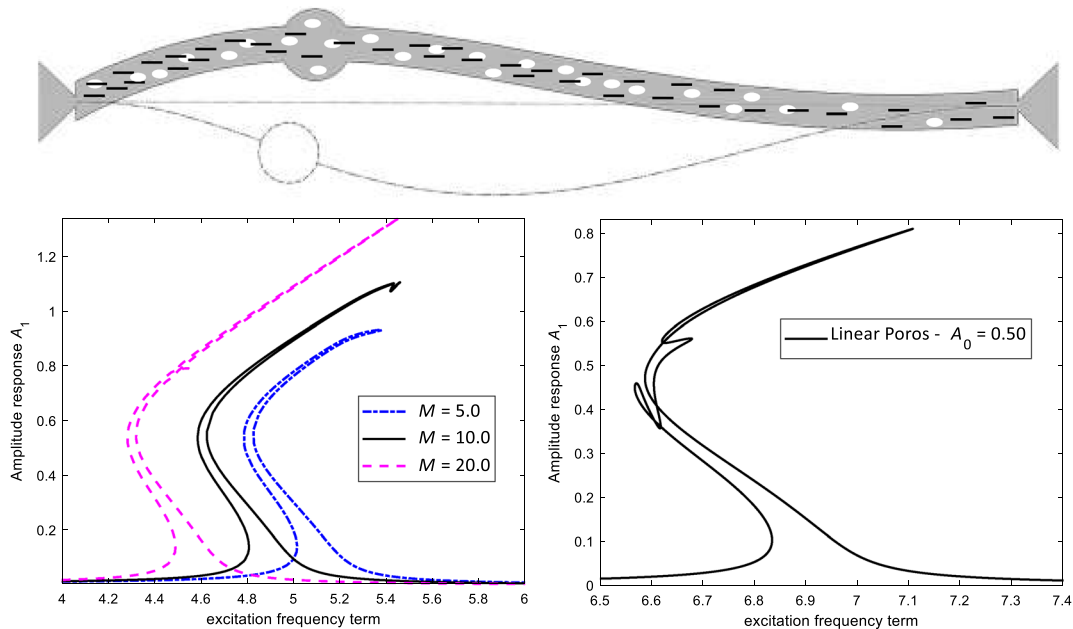
✉ Mergen H. Ghayesh  
mergen.ghayesh@adelaide.edu.au

<sup>1</sup> School of Mechanical Engineering, University of Adelaide,  
Adelaide, SA 5005, Australia

<sup>2</sup> Faculty of Science and Technology, University of Canberra,  
Canberra, Australia

<sup>3</sup> Department of Mechanical Engineering, McGill University,  
817 Sherbrooke Street West, Montreal, Canada

## Graphic abstract



**Keywords** Porosity · Nonlinear response · Nonlinear dynamics · Nonlinear vibration geometrical imperfection · Mass imperfection

## Abbreviations

$L$	Length of the beam
$b$	Width of the beam
$h$	Thickness of the beam
$M$	Mass imperfection parameter
$\alpha$	Porosity term
$E$	Young's modulus term
$\rho_i$	Mass density term
$k$	CNT grading power term
$u$	Axial displacement
$w$	Transverse displacement
$w_0$	Geometrical imperfection
$K$	The kinetic energy term
$U$	The potential energy term
$W_F$	The external work
$A$	Cross section of the beam
$I_i$	The area moments of inertia about the $z$ axis
$A_{11}, B_{11}, D_{11}$	Axial stiffness terms
$F$	External force
$\omega$	Excitation frequency term
$\Omega$	Nondimensional frequency term
$\gamma$	Slenderness ratio
$e_1$	Efficiency parameter
$x_0$	Position of the mass imperfection
$V_{CNT,total}$	Total volume fraction of CNT

$V_{CNT,left}$	CNT volume fraction at the left end
$V_m$	Volume fraction of matrix
$\nu$	Poisson's ratio
$t$	Time
$\delta_d$	Dirac delta
$\delta$	Variation symbol
$m$	Subscript referring to the matrix
$CNT$	Subscript referring to CNT

## 1 Introduction

With recent developments in various cross-disciplinary engineering fields, the importance of having optimum structures with higher durability-to-weight, stiffness-to-weight and strength-to-weight is visible in engineering horizon. Accordingly, numerous studies concentrated on strengthening conventional structures using different algorithms. Carbon-fibre, aramid-fibre and glass-fibre strengthened structures are some of the well-known outcomes of the research studies in this field [1–6]. Meanwhile, improvements in nano/micro-scale technologies made it possible to introduce carbon nanotubes (CNTs) as a reliable new reinforcement fibre [7–11]. CNTs are well-known for their spectacular mechanical, thermal, and electrical properties which made them an important element in different areas of science. Due to their ultra-small

scale, size-dependent effects and molecular interactions have been observed where modelled for different small-scale structures using nonlocal elasticity theories [12–24].

Moreover, the possibility to arrange the layout of fibres in CNT strengthened structures could make it flexible for designers to obtain different desirable mechanical behaviours in various applications of such structures. This importance could be achieved by functionally grading the fibres inside the matrix; however, to reach an efficient CNT distribution model for different purposes, it is necessary to comprehend the physical and mechanical properties of strengthened beams.

In the past few years, the mechanical response of CNT strengthened structures has been investigated by arranging the fibres through the thickness direction. For linear analysis, Lin and Xiang [25] investigated the free oscillation behaviour of functionally graded (FG) CNT strengthened beams. Shear deformable beam theories were used to model the beam and differences between the computed natural frequency terms were presented showing that by decreasing the CNT volume fraction, natural frequency terms decrease significantly compared to increasing the volume fraction. Shi et al. [26] analysed the effects of different types of boundary conditions on the linear oscillation of FG CNT reinforced beams; it was shown that the CNT distribution could affect the natural frequency terms significantly. Joshi et al. [27] analysed the strength and elasticity of CNT strengthened hexagonal section beams using finite-element simulation. Randomly dispersed and aligned CNTs were studied and it was shown that the effective elastic reinforcement is a function of CNT length and accordingly increasing the length of CNT fibres will increase the relative modulus term.

For large deformations and nonlinear analysis, Ke et al. [28] examined the nonlinear vibration behaviour of composite beams reinforced with single-walled carbon nanotubes (SWCNTs); the beam was modelled using Timoshenko beam theory and von Kármán geometry nonlinearity was taken into account—it was shown that the volume fraction and distribution of SWCNTs in the matrix could change the frequency ratio and mode shapes significantly. In another study, Pourasghar and Chen [29] investigated the effects of hyperbolic heat conduction on displacements and vibration response of CNT strengthened FG microbeams using Timoshenko beam theory and von Kármán geometry nonlinearity. It was concluded that linear and nonlinear frequencies decrease by increasing the thermal conductivity of the beam.

For analysing geometrical imperfection in CNT strengthened beams varying through the thickness, Wu et al. [30] studied the nonlinear oscillation response of composite beams strengthened with CNT; it was concluded that the nonlinear vibrations in the system is very sensitive to the initial imperfections.

Stability and buckling behaviour of strengthened beams with thickness FG CNT fibres have been examined by many researchers. Ke et al. [31] studied the dynamic stability of FG CNT strengthened beams by the means of differential quadrature method and Bolotin's technique highlighting that symmetric functionally graded CNT strengthened beams have higher excitation frequencies compared to the uniformly distributed model. In another study, Fattahi and Safaei [32] studied the buckling of functionally graded SWCNT strengthened beams with different boundary conditions where it was shown that decreasing the volume fraction of SWCNT causes smaller stiffness in the system.

Main concentration in the previous studies is on grading the CNTs through the thickness direction [25, 33, 34]. There have been few studies on analysing the influence of grading the CNTs along the length (AFG CNT strengthened beams) which focuses on the linear vibrations of the structure. In Ref. [35], authors analysed the linear vibration response of CNT strengthened beams. The beam was modelled by considering the influence of an elastic Winkler-Pasternak foundation and the linear natural frequencies were obtained using a generalised differential quadrature method (GDQM). Results were compared with literature and finite-element simulation for simplified models shown a great accuracy. In another study, the influence of imperfection on the linear vibrations of the beam was examined [36]. Different types of imperfections were considered and the results were obtained using a generalised decomposition technique. It was shown that the linear frequencies of the beam are sensitive to the distribution of CNTs and imperfections.

In this study, the effects of geometric nonlinearities on the coupled forced vibrations of AFG CNT reinforced beams are investigated in the presence of an external time-dependent transverse load with not neglecting axial motion (Fig. 1); this is for the first time. The coupled equation of motion is adopted from Ref. [36] and the non-dimensional form and the solution procedure are presented in details. General forms of functionally graded CNT distributions are presented for modelling the reinforcement in the structure. The governing equations are solved using a combination of Galerkin scheme and dynamic equilibrium technique, and a comprehensive parametric study on the nonlinear vibrations of the structure is conducted by considering different types of porosities and imperfections.

## 2 Problem definition and solution procedure

### 2.1 Model description

The coupled equations of motion of geometrical/mass imperfect porous CNT strengthened beams have previously

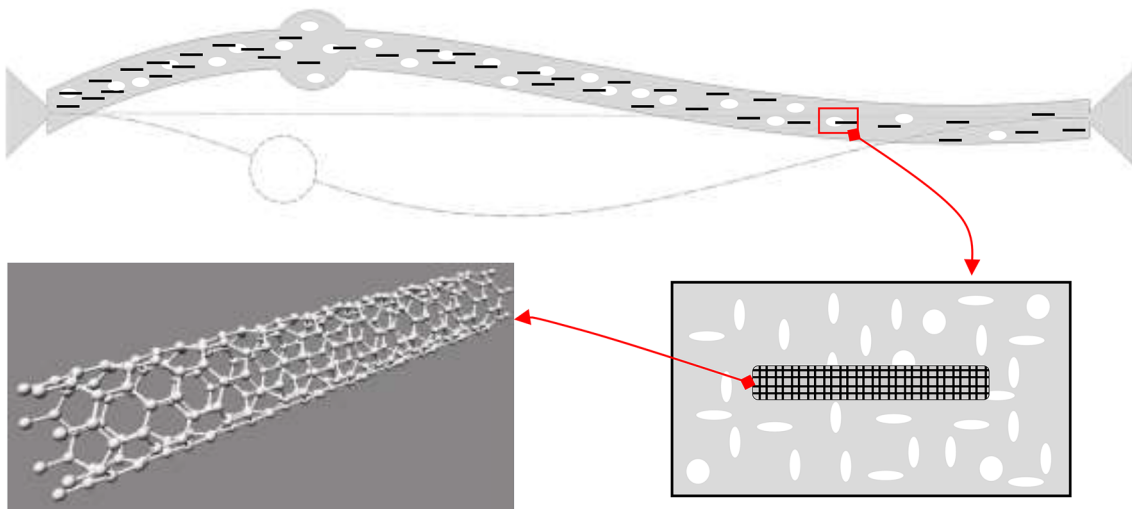


**Fig. 1** Schematic representation of porous axially functionally graded CNT strengthened beams with geometric and mass imperfections

been obtained in Ref. [36], by the same authors which by adding the presence of an external harmonic load, is briefly described here. For a hollow beam model, by having a

geometrical imperfection and neglecting the shear deformation, variations of potential and kinetic energy terms are written as

$$\begin{aligned}
 \delta U = & \int_0^L \int_A \frac{E(x, z)}{1 - \nu^2(x)} \left[ \frac{\partial u(x, t)}{\partial x} - z \frac{\partial^2 w(x, t)}{\partial x^2} + \frac{1}{2} \left( \frac{\partial w(x, t)}{\partial x} \right)^2 \right. \\
 & \left. + \frac{\partial w(x, t)}{\partial x} \frac{dw_0(x)}{dx} \right] \delta \left( \frac{\partial u(x, t)}{\partial x} \right) dA dx \\
 & - \int_0^L \int_A z \frac{E(x, z)}{1 - \nu^2(x)} \left[ \frac{\partial u(x, t)}{\partial x} + \frac{1}{2} \left( \frac{\partial w(x, t)}{\partial x} \right)^2 - z \frac{\partial^2 w(x, t)}{\partial x^2} \right. \\
 & \left. + \frac{\partial w(x, t)}{\partial x} \frac{dw_0(x)}{dx} \right] \delta \left( \frac{\partial^2 w(x, t)}{\partial x^2} \right) dA dx \\
 & + \int_0^L \int_A \frac{E(x, z)}{1 - \nu^2(x)} \left( \frac{\partial w(x, t)}{\partial x} \right) \left[ \frac{\partial u(x, t)}{\partial x} + \frac{1}{2} \left( \frac{\partial w(x, t)}{\partial x} \right)^2 - z \frac{\partial^2 w(x, t)}{\partial x^2} \right. \\
 & \left. + \frac{\partial w(x, t)}{\partial x} \frac{dw_0(x)}{dx} \right] \delta \left( \frac{\partial w(x, t)}{\partial x} \right) dA dx \\
 & + \int_0^L \int_A \frac{E(x, z)}{1 - \nu^2(x)} \left( \frac{dw_0(x)}{dx} \right) \left[ \frac{\partial u(x, t)}{\partial x} - z \frac{\partial^2 w(x, t)}{\partial x^2} + \frac{1}{2} \left( \frac{\partial w(x, t)}{\partial x} \right)^2 \right. \\
 & \left. + \frac{\partial w(x, t)}{\partial x} \frac{dw_0(x)}{dx} \right] \delta \left( \frac{\partial w(x, t)}{\partial x} \right) dA dx
 \end{aligned} \tag{1}$$

$$\begin{aligned}
 \delta K = & M \int_0^L \left[ \frac{\partial u(x,t)}{\partial t} \delta \left( \frac{\partial u(x,t)}{\partial t} \right) + \frac{\partial w(x,t)}{\partial t} \delta \left( \frac{\partial w(x,t)}{\partial t} \right) \right] \delta_d(x-x_0) dx \\
 & - \int_0^L \int_A \rho(x,z) z \left[ \left( \frac{\partial u(x,t)}{\partial t} - z \frac{\partial^2 w(x,t)}{\partial x \partial t} \right) \delta \left( \frac{\partial^2 w(x,t)}{\partial x \partial t} \right) \right] dA dx \\
 & + \int_0^L \int_A \rho(x,z) \left[ \left( \frac{\partial u(x,t)}{\partial t} - z \frac{\partial^2 w(x,t)}{\partial x \partial t} \right) \delta \left( \frac{\partial u(x,t)}{\partial t} \right) \right] dA dx \\
 & + \int_0^L \int_A \rho(x,z) \left[ \frac{\partial w(x,t)}{\partial t} \delta \left( \frac{\partial w(x,t)}{\partial t} \right) \right] dA dx,
 \end{aligned} \tag{2}$$

where  $E$  is the Young’s modulus (function of  $x$  and  $z$ ),  $\nu$  is the Poisson ratio (function of  $x$ ),  $\rho$  is the density (function of  $x$  and  $z$ ),  $w$  and  $u$  are the transverse and axial displacements in  $z$  and  $x$  directions, respectively,  $w_0$  is the geometrical imperfection,  $M$  is the lumped mass imperfection,  $x_0$  is the axial position of the mass imperfection,  $A$  is the cross section,  $t$  is time,  $L$  is the length of the beam,  $\delta_d$  is the Dirac delta, and  $\delta$  is the variation symbol. For the sake of brevity, the procedure for obtaining Eqs. (1) and (2) is shown in

Appendix A. The variation of the external work ( $W_F$ ) due to a transverse external harmonic excitation force is

$$\delta W_F = \int_0^L F \cos(\omega t) \delta w dx, \tag{3}$$

where  $F$  is the external force magnitude and  $\omega$  is the frequency of the harmonic excitation. Employing the coupled equations of motion, Hamilton’s principle gives [36]

$$\begin{aligned}
 & \frac{\partial}{\partial x} \left[ A_{11}(x) \frac{\partial u(x,t)}{\partial x} \right] - M \left[ \frac{\partial^2 u(x,t)}{\partial t^2} \right] \delta(x-x_0) - \frac{\partial}{\partial x} \left[ B_{11}(x) \frac{\partial^2 w(x,t)}{\partial x^2} \right] \\
 & + \frac{1}{2} \frac{\partial}{\partial x} \left[ A_{11}(x) \left( \frac{\partial w(x,t)}{\partial x} \right)^2 \right] + \frac{\partial}{\partial x} \left[ A_{11}(x) \left( \frac{\partial w(x,t)}{\partial x} \right) \left( \frac{dw_0(x)}{dx} \right) \right] \\
 & = I_0(x) \left( \frac{\partial^2 u(x,t)}{\partial t^2} \right) - I_1(x) \left( \frac{\partial^3 w(x,t)}{\partial x \partial t^2} \right),
 \end{aligned} \tag{4}$$

$$\begin{aligned}
 & - \frac{\partial^2}{\partial x^2} \left[ D_{11}(x) \frac{\partial^2 w(x,t)}{\partial x^2} \right] - \frac{\partial}{\partial x} \left[ B_{11}(x) \frac{\partial^2 w(x,t)}{\partial x^2} \frac{\partial w(x,t)}{\partial x} \right] - \frac{\partial}{\partial x} \left[ B_{11}(x) \frac{\partial^2 w(x,t)}{\partial x^2} \frac{dw_0(x)}{dx} \right] \\
 & + \frac{\partial^2}{\partial x^2} \left[ B_{11}(x) \frac{\partial u(x,t)}{\partial x} \right] + \frac{\partial^2}{\partial x^2} \left[ B_{11}(x) \frac{dw_0(x)}{dx} \frac{\partial w(x,t)}{\partial x} \right] \\
 & + \frac{\partial}{\partial x} \left[ A_{11}(x) \frac{\partial u(x,t)}{\partial x} \frac{dw_0(x)}{dx} \right] + \frac{1}{2} \frac{\partial}{\partial x} \left[ A_{11}(x) \frac{\partial w(x,t)}{\partial x} \left( \frac{\partial w(x,t)}{\partial x} \right)^2 \right] \\
 & + \frac{\partial}{\partial x} \left[ A_{11}(x) \frac{\partial w(x,t)}{\partial x} \frac{\partial u(x,t)}{\partial x} \right] - M \left( \frac{\partial^2 w(x,t)}{\partial t^2} \right) \delta(x-x_0) \\
 & + \frac{1}{2} \frac{\partial}{\partial x} \left[ A_{11}(x) \left( \frac{\partial w(x,t)}{\partial x} \right)^2 \frac{dw_0(x)}{dx} \right] + \frac{1}{2} \frac{\partial^2}{\partial x^2} \left[ B_{11}(x) \left( \frac{\partial w(x,t)}{\partial x} \right)^2 \right] \\
 & + \frac{\partial}{\partial x} \left[ A_{11}(x) \left( \frac{\partial w(x,t)}{\partial x} \right)^2 \frac{dw_0(x)}{dx} \right] + \frac{\partial}{\partial x} \left[ A_{11}(x) \frac{\partial w(x,t)}{\partial x} \left( \frac{dw_0(x)}{dx} \right)^2 \right] \\
 & = I_0(x) \frac{\partial^2 w(x,t)}{\partial t^2} + \frac{\partial}{\partial x} \left[ I_1(x) \frac{\partial^2 u(x,t)}{\partial t^2} \right] - \frac{\partial}{\partial x} \left[ I_2(x) \frac{\partial^3 w(x,t)}{\partial x \partial t^2} \right] + F \cos(\omega t),
 \end{aligned} \tag{5}$$

with the axial stiffness terms ( $D_{11}$ ,  $B_{11}$  and  $A_{11}$ ) and the area moments of inertia ( $I_2$ ,  $I_1$  and  $I_0$ ) about the  $z$  axis defined as [36]

$$\begin{bmatrix} I_2(x) \\ I_1(x) \\ I_0(x) \end{bmatrix} = \int_{-h/2}^{h/2} b \begin{bmatrix} z^2 \\ z \\ 1 \end{bmatrix} \left\{ \rho_m - \alpha_2(z) [V_{CNT}(x)\rho_{CNT} + V_m(x)\rho_m] + V_{CNT}(x)(\rho_{CNT} - \rho_m) \right\} dz, \tag{6}$$

$$\begin{bmatrix} D_{11}(x) \\ B_{11}(x) \\ A_{11}(x) \end{bmatrix} = \int_{-h/2}^{h/2} b \begin{bmatrix} z^2 \\ z \\ 1 \end{bmatrix} \left\{ \frac{E_m - \alpha_1(z) [V_{CNT}(x)e_1 E_{CNT} + V_m(x)E_m] + V_{CNT}(x)(e_1 E_{CNT} - E_m)}{1 - \nu^2(x)} \right\} dz, \tag{7}$$

where subscripts  $m$  and  $CNT$  denote the matrix and CNT properties,  $V$  is the volume fraction and  $e_1$  is the effective coefficient indicating the efficiency of CNTs in strengthening the Young’s modulus of the composite, and  $\alpha_1$  and  $\alpha_1$  are the porosity terms affecting the Young’s modulus and density

terms respectively. For symmetric porosity variation through the thickness, the stiffness and inertia terms  $B_{11}$  and  $I_1$  will be zero.

### 2.2 Solution method

Since the equations of motion include different parameters with a wide range of scale, new non-dimensional parameters are defined to decrease the scale differences as [36]

$$\begin{aligned} w^* &= \frac{w}{h}, \quad w_0^* = \frac{w_0}{h}, \quad u^* = \frac{u}{h}, \quad x^* = \frac{x}{L}, \quad x_0^* = \frac{x_0}{L}, \quad z^* = \frac{z}{h}, \quad \Omega = \omega \sqrt{\frac{L^4 I_{0,m}}{D_{11,m}}} \\ t^* &= \sqrt{\frac{D_{11,m}}{L^4 I_{0,m}}} t, \quad \gamma = \sqrt{\frac{L}{h}}, \quad I_0^* = \frac{I_0}{I_{0,m}}, \quad I_1^* = \frac{I_1}{I_{0,m}L}, \quad I_2^* = \frac{I_2}{I_{0,m}L^2}, \\ A_{11}^* &= h^2 \frac{A_{11}}{D_{11,m}}, \quad B_{11}^* = h \frac{B_{11}}{D_{11,m}}, \quad D_{11}^* = \frac{D_{11}}{D_{11,m}}, \quad F^* = \frac{FL^4}{D_{11,m}h}, \quad M^* = \frac{M}{I_{0,m}L}, \end{aligned} \tag{8}$$

and the nonlinear coupled Eqs. (4) and (5) are rewritten using the non-dimensional parameters in Eq. (8) as

$$\begin{aligned} & -I_0(x) \left( \frac{\partial u^2(x,t)}{\partial t^2} \right) + I_1(x) \left( \frac{\partial^3 w(x,t)}{\partial x \partial t^2} \right) \\ & + \frac{\partial}{\partial x} \left\{ A_{11}(x) \left[ \gamma^4 \frac{\partial u(x,t)}{\partial x} + \frac{1}{2} \gamma^2 \left( \frac{\partial w(x,t)}{\partial x} \right)^2 + \gamma^2 \left( \frac{\partial w(x,t)}{\partial x} \right) \left( \frac{dw_0(x)}{dx} \right) \right] \right\} \\ & - \frac{\partial}{\partial x} \left\{ B_{11}(x) \gamma^2 \left[ \frac{\partial^2 w(x,t)}{\partial x^2} \right] \right\} - M \left( \frac{\partial^2 u(x,t)}{\partial t^2} \right) \delta(x - x_0) = 0, \end{aligned} \tag{9}$$

$$\begin{aligned}
 & -I_0(x) \left( \frac{\partial^2 w(x, t)}{\partial t^2} \right) + \frac{\partial}{\partial x} \left[ I_2(x) \left( \frac{\partial^3 w(x, t)}{\partial x \partial t^2} \right) \right] - \frac{\partial}{\partial x} \left[ I_1(x) \left( \frac{\partial^2 u(x, t)}{\partial t^2} \right) \right] \\
 & - \frac{\partial^2}{\partial x^2} \left\{ D_{11}(x) \left[ \frac{\partial^2 w(x, t)}{\partial x^2} \right] \right\} - \frac{\partial}{\partial x} \left\{ B_{11}(x) \left[ \frac{\partial^2 w(x, t)}{\partial x^2} \right] \left( \frac{\partial w(x, t)}{\partial x} + \frac{dw_0(x)}{dx} \right) \right\} \\
 & + \frac{\partial^2}{\partial x^2} \left\{ B_{11}(x) \left[ \frac{1}{2} \left( \frac{\partial w(x, t)}{\partial x} \right)^2 + \gamma^2 \frac{\partial u(x, t)}{\partial x} + \left( \frac{\partial w(x, t)}{\partial x} \right) \left( \frac{dw_0(x)}{dx} \right) \right] \right\} \\
 & + \frac{\partial}{\partial x} \left\{ A_{11}(x) \left[ \gamma^2 \frac{\partial u(x, t)}{\partial x} + \frac{1}{2} \left( \frac{\partial w(x, t)}{\partial x} \right)^2 \right] \left( \frac{\partial w(x, t)}{\partial x} + \frac{dw_0(x)}{dx} \right) \right\} \\
 & + \frac{\partial}{\partial x} \left\{ A_{11}(x) \left( \frac{dw_0(x)}{dx} \frac{\partial w(x, t)}{\partial x} \right) \left( \frac{\partial w(x, t)}{\partial x} + \frac{dw_0(x)}{dx} \right) \right\} \\
 & - M \left( \frac{\partial^2 w(x, t)}{\partial t^2} \right) \delta(x - x_0) = F \cos(\Omega t).
 \end{aligned} \tag{10}$$

The superscript \* is removed from Eqs. (9) and (10) for the sake of brevity. The axial and transverse motion of the hollow beam are written by assuming the first  $2N$  modes of vibration and neglecting the shear effects using Galerkin’s scheme as

$$u(x, t) = \sum_{j=1}^N r_j(t) \phi_j(x), \tag{11}$$

$$w(x, t) = \sum_{i=1}^N p_i(t) \psi_i(x), \tag{12}$$

the governing coupled Eqs. (9) and (10) are rewritten as

$$\begin{aligned}
 & I_0(x) \sum_{i=1}^N \phi_i \ddot{r}_i(t) + M \sum_{i=1}^N \phi_i \delta(x - x_0) \ddot{r}_i(t) - I_1(x) \sum_{i=1}^N \left( \frac{d\psi_i}{dx} \right) \ddot{p}_i(t) \\
 & - \frac{d}{dx} \left[ A_{11}(x) \gamma^4 \sum_{i=1}^N \left( \frac{d\phi_i}{dx} \right) \right] r_i(t) \\
 & - \frac{d}{dx} \left\{ A_{11}(x) \gamma^2 \sum_{i=1}^N \left( \frac{d\psi_0}{dx} \right) \left( \frac{d\psi_i}{dx} \right) - B_{11}(x) \gamma^2 \sum_{i=1}^N \left( \frac{d^2\psi_i}{dx^2} \right) \right\} p_i(t) \\
 & - \frac{d}{dx} \left\{ \frac{1}{2} A_{11}(x) \gamma^2 \sum_{i=1}^N \sum_{j=1}^N \left( \frac{d\psi_i}{dx} \right) \left( \frac{d\psi_j}{dx} \right) \right\} p_i(t) p_j(t) = 0,
 \end{aligned} \tag{13}$$

$$\begin{aligned}
 I_0(x) \sum_{i=1}^N \psi_i \ddot{p}_i(t) + M \sum_{i=1}^N \psi_i \delta(x - x_0) \ddot{p}_i(t) - \frac{d}{dx} \left[ I_2(x) \sum_{i=1}^N \left( \frac{d\psi_i}{dx} \right) \right] \ddot{p}_i(t) + \frac{d}{dx} \left[ I_1(x) \sum_{i=1}^N \phi_i \right] \ddot{r}_i(t) \\
 + \frac{d^2}{dx^2} \left\{ D_{11}(x) \sum_{i=1}^N \left( \frac{d^2\psi_i}{dx^2} \right) \right\} p_i(t) + \frac{d}{dx} \left\{ B_{11}(x) \sum_{i=1}^N \left( \frac{d\psi_0}{dx} \right) \left( \frac{d^2\psi_i}{dx^2} \right) \right\} p_i(t) \\
 - \frac{d^2}{dx^2} \left\{ B_{11}(x) \sum_{i=1}^N \left( \frac{d\psi_0}{dx} \right) \left( \frac{d\psi_i}{dx} \right) \right\} p_i(t) - \frac{d}{dx} \left\{ A_{11}(x) \sum_{i=1}^N \left( \frac{d\psi_0}{dx} \right)^2 \left( \frac{d\psi_i}{dx} \right) \right\} p_i(t) \\
 - \frac{d}{dx} \left\{ A_{11}(x) \gamma^2 \sum_{i=1}^N \left( \frac{d\psi_0}{dx} \right) \left( \frac{d\phi_i}{dx} \right) \right\} r_i(t) - \frac{d^2}{dx^2} \left\{ B_{11}(x) \gamma^2 \sum_{i=1}^N \left( \frac{d\phi_i}{dx} \right) \right\} r_i(t) \\
 + \frac{d}{dx} \left\{ B_{11}(x) \sum_{j=1}^N \sum_{i=1}^N \left( \frac{d\psi_i}{dx} \right) \left( \frac{d^2\psi_j}{dx^2} \right) \right\} p_i(t) p_j(t) \\
 - \frac{d^2}{dx^2} \left\{ \frac{1}{2} B_{11}(x) \sum_{i=1}^N \sum_{j=1}^N \left( \frac{d\psi_i}{dx} \right) \left( \frac{d\psi_j}{dx} \right) \right\} p_i(t) p_j(t) \\
 - \frac{d}{dx} \left\{ \frac{3}{2} A_{11}(x) \sum_{i=1}^N \sum_{j=1}^N \left( \frac{d\psi_0}{dx} \right) \left( \frac{d\psi_i}{dx} \right) \left( \frac{d\psi_j}{dx} \right) \right\} p_i(t) p_j(t) \\
 - \frac{d}{dx} \left\{ A_{11}(x) \gamma^2 \sum_{i=1}^N \sum_{j=1}^N \left( \frac{d\phi_i}{dx} \right) \left( \frac{d\psi_j}{dx} \right) \right\} r_i(t) p_j(t) \\
 - \frac{d}{dx} \left\{ \frac{1}{2} A_{11}(x) \sum_{i=1}^N \sum_{j=1}^N \sum_{k=1}^N \left( \frac{d\psi_i}{dx} \right) \left( \frac{d\psi_j}{dx} \right) \left( \frac{d\psi_k}{dx} \right) \right\} p_i(t) p_j(t) p_k(t) = F \cos(\Omega t),
 \end{aligned} \tag{14}$$

which can be sorted as

$$M_{11}\ddot{r} + M_{12}\ddot{p} + C_1\dot{r} + KL_{11}r + KL_{12}p + KN_{11}p^2 = 0, \tag{15}$$

$$M_{22}\ddot{p} + M_{21}\ddot{r} + C_2\dot{p} + KL_{21}r + KL_{22}p + KN_{21}p^2 + KN_{22}rp + KN_{23}p^3 = F, \tag{16}$$

with

$$r = [r_1, r_2, r_3, \dots, r_N], \tag{17} \quad KN_{11}(l, i, j) = - \int_0^1 \varphi_l(x) \frac{d}{dx} \left\{ \frac{1}{2} A_{11}(x) \gamma^2 \left( \frac{d\psi_i}{dx} \right) \left( \frac{d\psi_j}{dx} \right) \right\} dx, \tag{19}$$

$$\begin{aligned}
 p = [p_1, p_2, p_3, \dots, p_N], \tag{18} \\
 KN_{21}(l, i, j) = \int_0^1 \psi_l \frac{d}{dx} \left\{ B_{11}(x) \left( \frac{d\psi_i}{dx} \right) \left( \frac{d^2\psi_j}{dx^2} \right) \right\} dx \\
 - \int_0^1 \psi_l \frac{d^2}{dx^2} \left\{ \frac{1}{2} B_{11}(x) \left( \frac{d\psi_i}{dx} \right) \left( \frac{d\psi_j}{dx} \right) \right\} dx \\
 - \int_0^1 \psi_l \frac{d}{dx} \left\{ \frac{3}{2} A_{11}(x) \left( \frac{d\psi_0}{dx} \right) \left( \frac{d\psi_i}{dx} \right) \left( \frac{d\psi_j}{dx} \right) \right\} dx,
 \end{aligned} \tag{20}$$



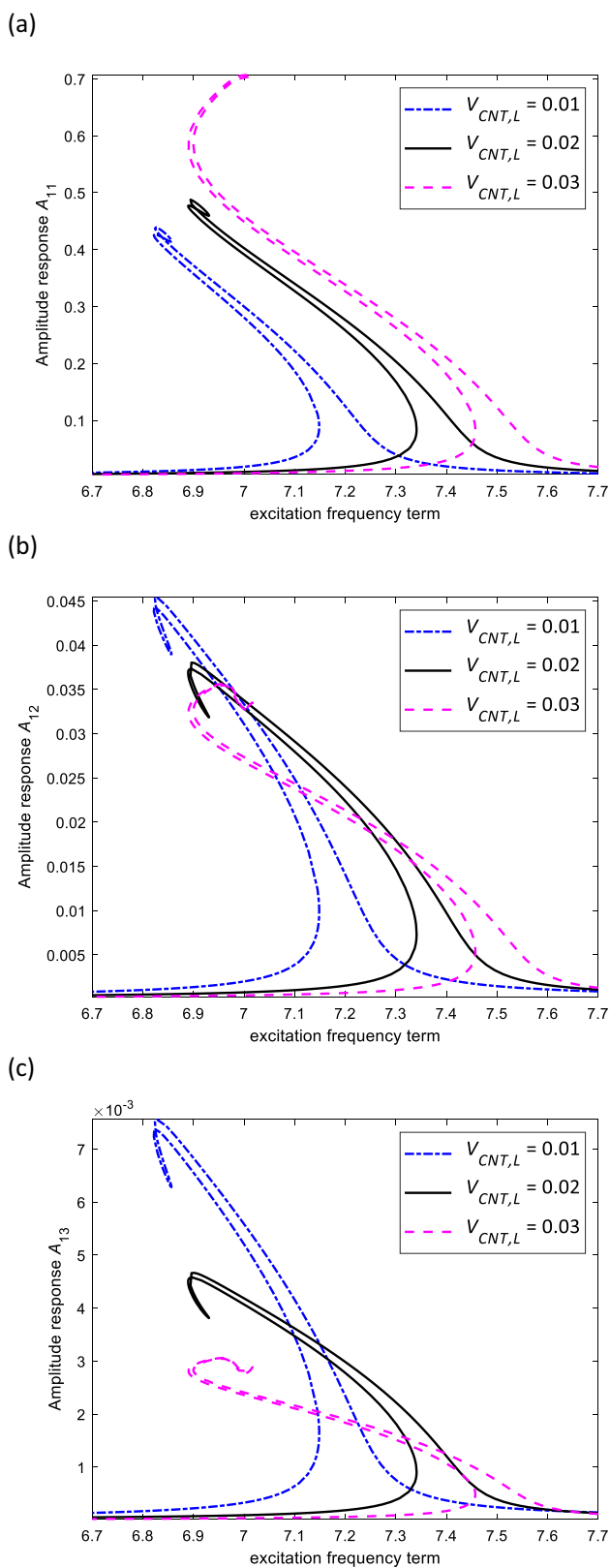


**Fig. 2** Influence of the CNT fibre distribution through the length on the *transverse* amplitude-frequency response of imperfect AFG CNT strengthened porous beam **a**  $V_{CNT,L}=1\%$ , **b**  $V_{CNT,L}=2\%$ , and **c**  $V_{CNT,L}=3\%$

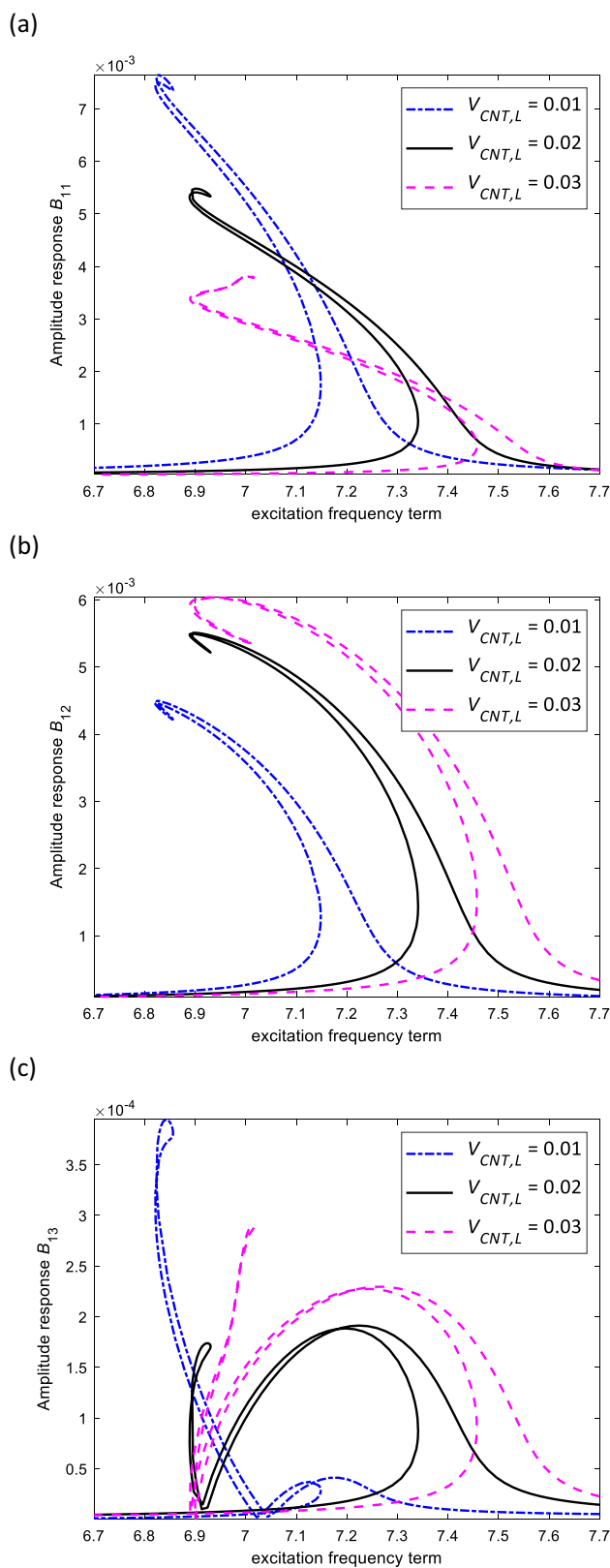


**Fig. 3** Influence of the CNT fibre distribution through the length on the *axial* amplitude-frequency response of imperfect AFG CNT strengthened porous beam **a**  $V_{CNT,L}=1\%$ , **b**  $V_{CNT,L}=2\%$ , and **c**  $V_{CNT,L}=3\%$

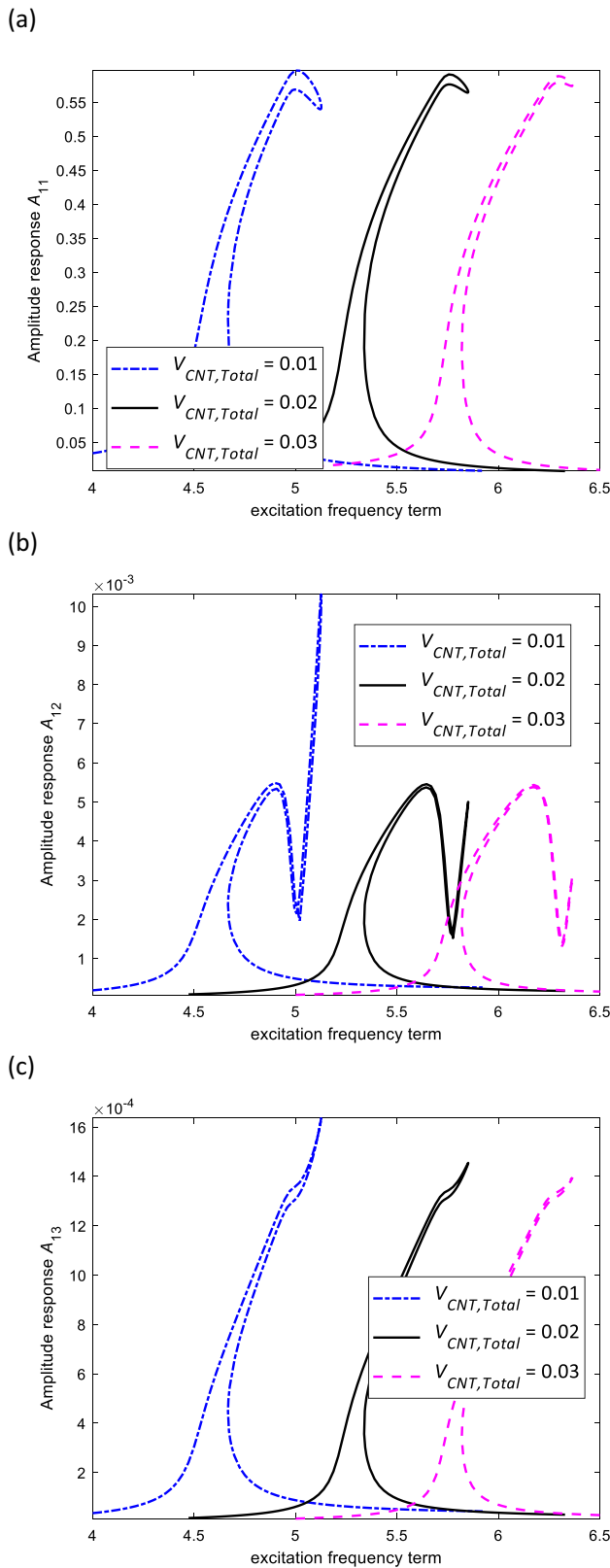


**Fig. 4** Influence of the total volume of CNT fibre on the *transverse* amplitude-frequency response of imperfect AFG CNT strengthened porous beam **a**  $V_{CNT,Total} = 1\%$ , **b**  $V_{CNT,Total} = 2\%$ , and **c**  $V_{CNT,Total} = 3\%$

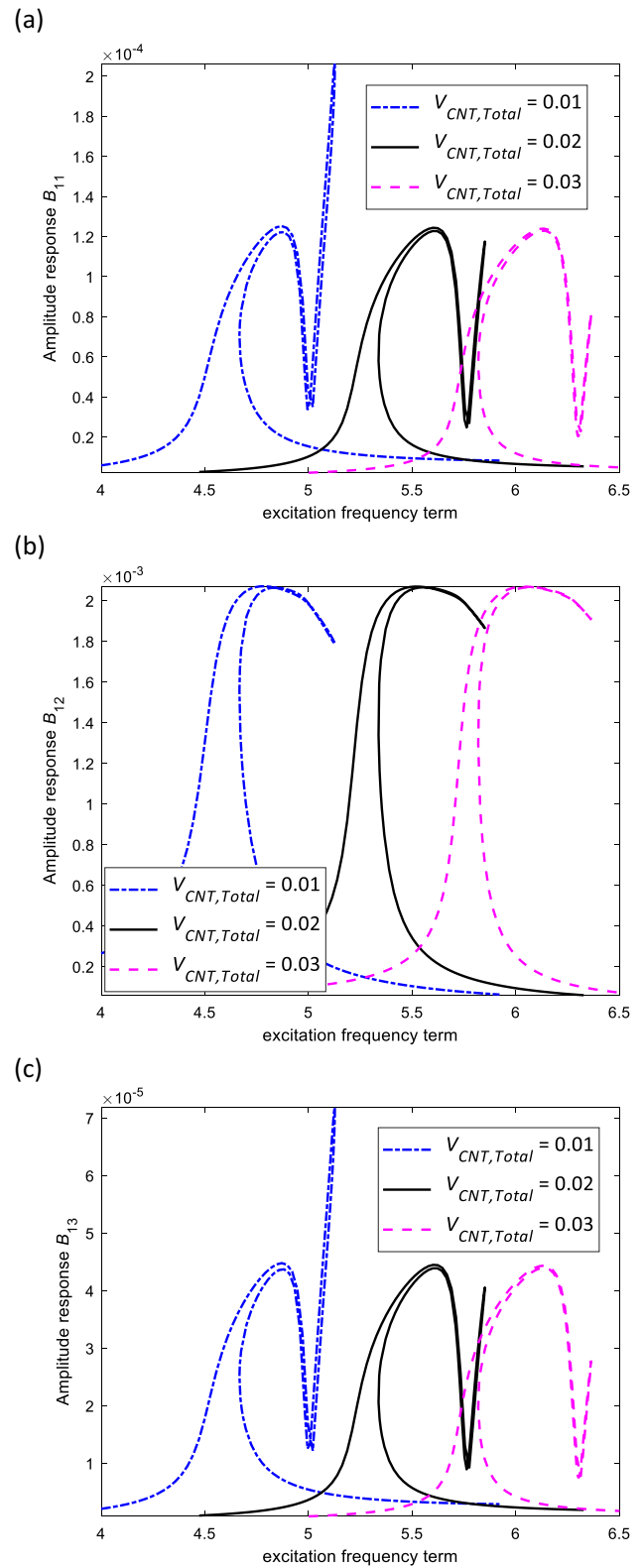


**Fig. 5** Influence of the total volume of CNT fibre on the *axial* amplitude-frequency response of imperfect AFG CNT strengthened porous beam **a**  $V_{CNT,Total} = 1\%$ , **b**  $V_{CNT,Total} = 2\%$ , and **c**  $V_{CNT,Total} = 3\%$

$$KN_{22}(l, i, j) = - \int_0^1 \psi_l \frac{d}{dx} \left\{ A_{11}(x) \gamma^2 \left( \frac{d\phi_i}{dx} \right) \left( \frac{d\psi_j}{dx} \right) \right\} dx, \tag{21}$$

$$KN_{23}(l, i, j, k) = - \int_0^1 \psi_l \frac{d}{dx} \left\{ \frac{1}{2} A_{11}(x) \left( \frac{d\psi_i}{dx} \right) \left( \frac{d\psi_j}{dx} \right) \left( \frac{d\psi_k}{dx} \right) \right\} dx, \tag{22}$$

and the linear coefficients  $M_{11}$ ,  $M_{12}$ ,  $KL_{11}$ ,  $KL_{12}$ ,  $KL_{21}$  and  $KL_{22}$  are given in Ref. [31]. Using the given assumptions and employing a dynamic equilibrium technique for appropriate beam base functions, the dynamic equilibrium coefficients are written in an exponential series as

$$p_n = \sum_{m=-N}^N A_{mn} e^{in\Omega t}, \tag{23}$$

$$r_n = \sum_{m=-N}^N B_{mn} e^{in\Omega t}, \tag{24}$$

where  $A_{mn}$  and  $B_{mn}$  are the dynamic equilibrium coordinates and the dynamic complex equilibrium equation are obtained by substituting Eqs. (23) and (24) into Eqs. (15) and (16) as [37]

$$\begin{aligned} & \left\{ -n^2 \Omega^2 [M] + in\Omega [C] + [K] \right\} \begin{Bmatrix} r_n \\ p_n \end{Bmatrix} \\ & = \begin{Bmatrix} 0 \\ F_n^{\text{external}} \end{Bmatrix} + \begin{Bmatrix} NL1_n^{\text{system}} \\ NL2_n^{\text{system}} \end{Bmatrix}, \end{aligned} \tag{25}$$

where  $F_n^{\text{external}}$  is the external actuating force on each mode of transverse motion, and  $NL1_n^{\text{system}}$  and  $NL2_n^{\text{system}}$  are the non-linear terms of the axial and transverse motions, respectively. By considering all the  $2N$  modes of vibration in axial and transverse equations, Eq. (25) is rewritten as

$$[T]\{R\} = \{F^{\text{external}}\} + \{NL^{\text{system}}\}, \tag{26}$$

where  $[T]$  is a complex matrix defined and  $\{R\}$  is the amplitudes of the motion defined as

$$[T] = \left\{ -n^2 \Omega^2 [M] + in\Omega [C] + [K] \right\}, \tag{27}$$

$$\{R\} = \begin{Bmatrix} r \\ p \end{Bmatrix}. \tag{28}$$

For the next step, using Eq. (26), an equivalent root-finding equation is written as

$$G(R, \Omega) = [T]\{R\} - \{F^{\text{external}}\} - \{NL^{\text{system}}\} = 0, \tag{29}$$

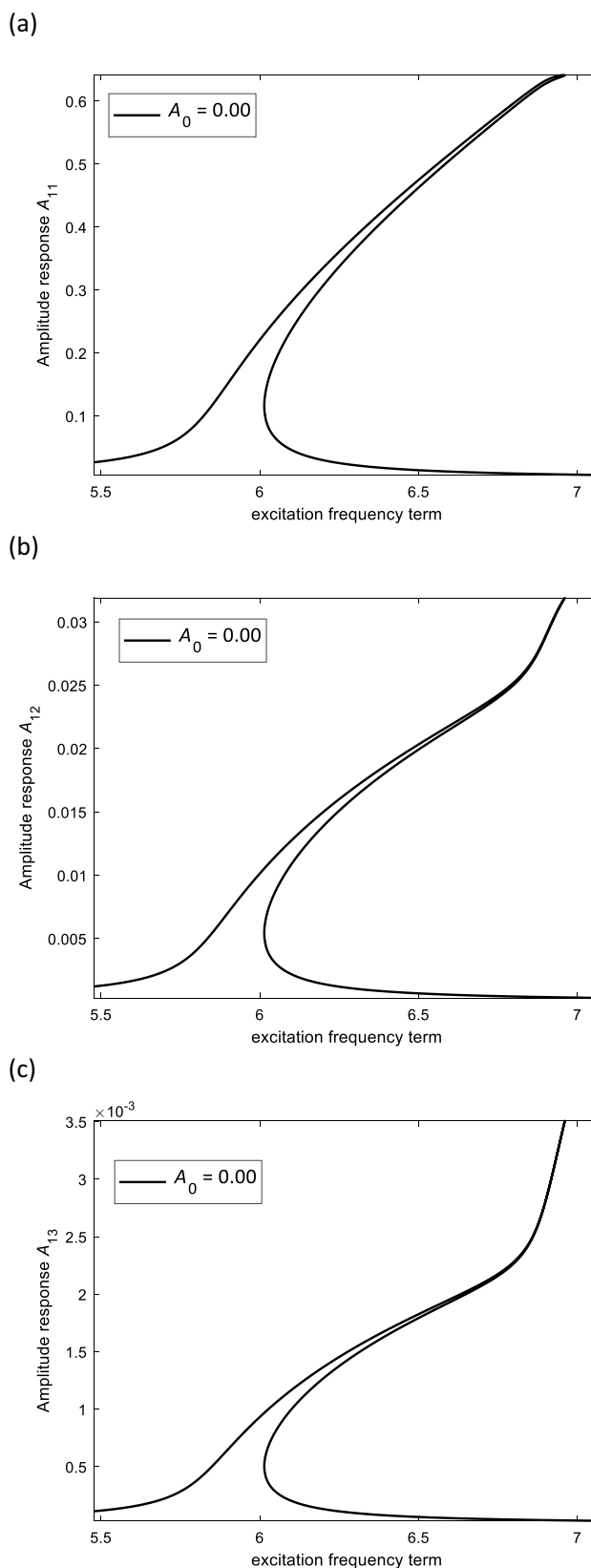


**Fig. 6** Transverse amplitude-frequency response of geometrically perfect AFG CNT strengthened porous beam (uniform open-cell porosity with  $\alpha_1=0.4$ ) **a** first coordinate, **b** second coordinate, and **c** third coordinate

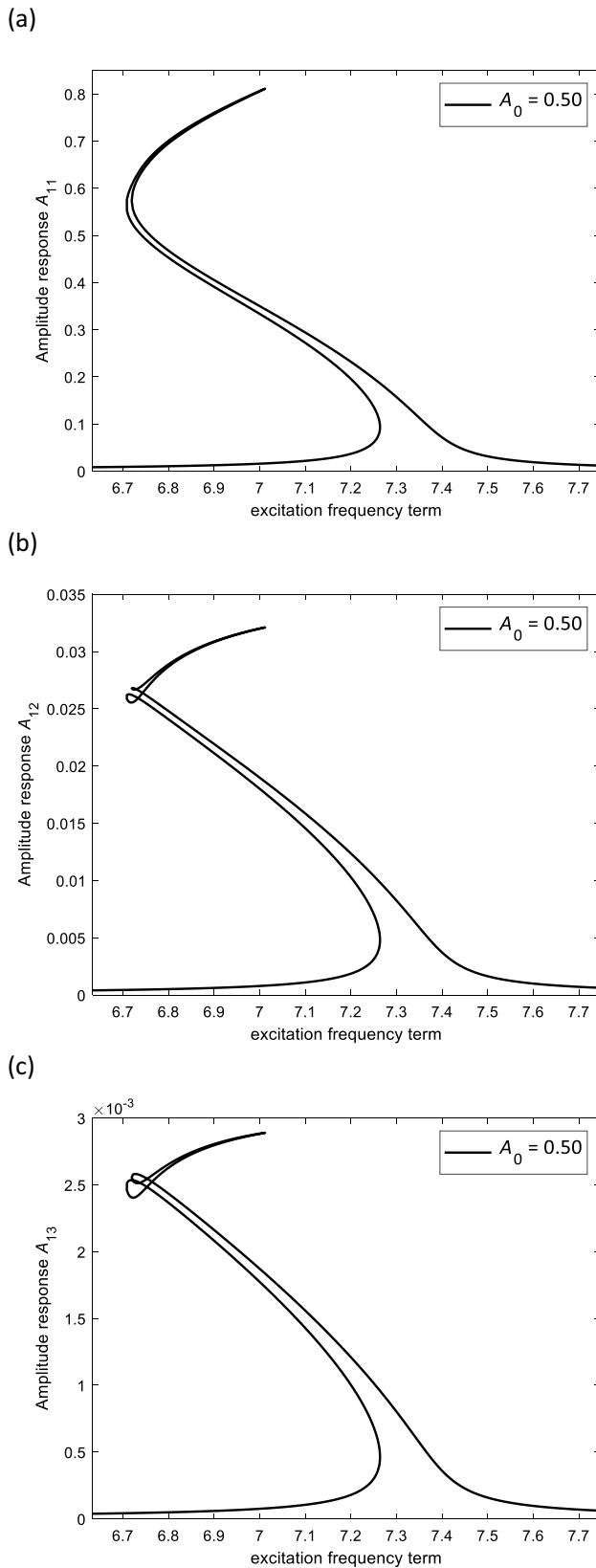


**Fig. 7** Transverse amplitude-frequency response of geometrically imperfect ( $A_0=0.5$ ) AFG CNT strengthened porous beam (uniform open-cell porosity with  $\alpha_1=0.4$ ) **a** first coordinate, **b** second coordinate, and **c** third coordinate

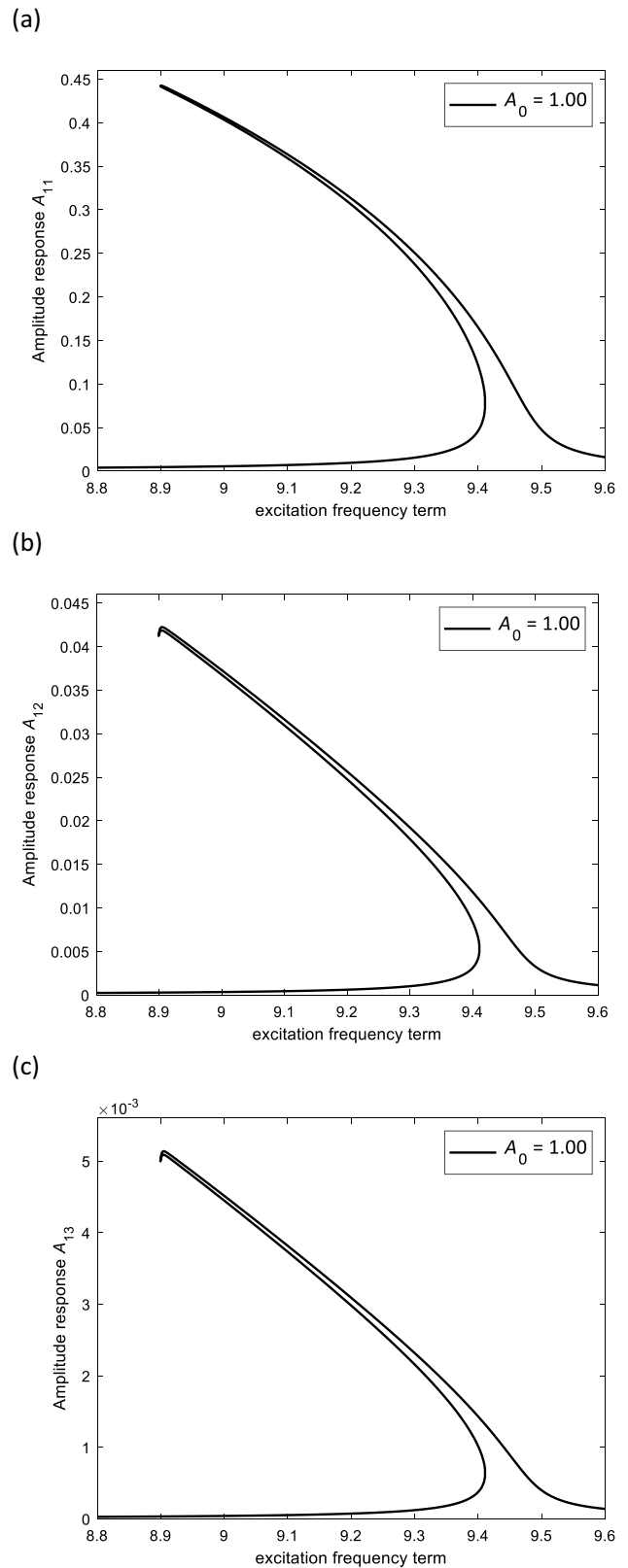


**Fig. 8** Transverse amplitude-frequency response of geometrically imperfect ( $A_0=1.0$ ) AFG CNT strengthened porous beam (uniform open-cell porosity with  $\alpha_1=0.4$ ) **a** first coordinate, **b** second coordinate, and **c** third coordinate

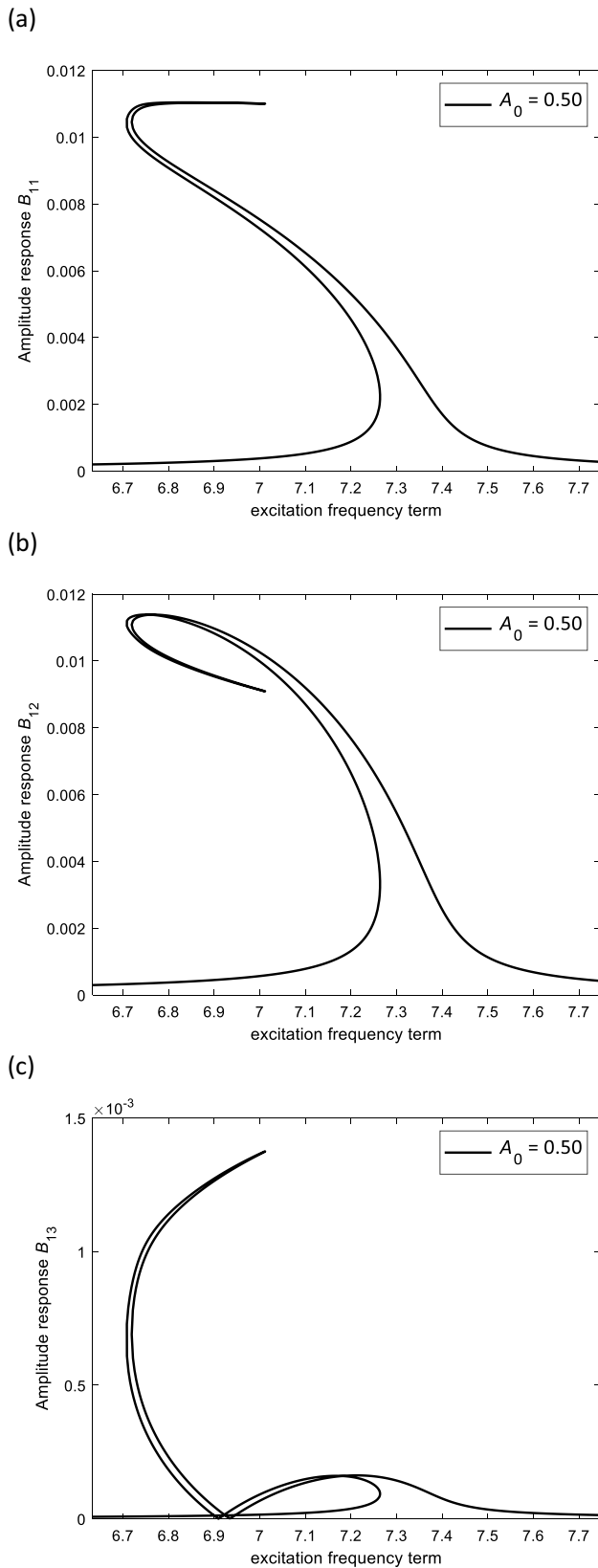


**Fig. 9** Axial amplitude-frequency response of geometrically imperfect ( $A_0=0.5$ ) AFG CNT strengthened porous beam (uniform open-cell porosity with  $\alpha_1=0.4$ ) **a** first coordinate, **b** second coordinate, and **c** third coordinate

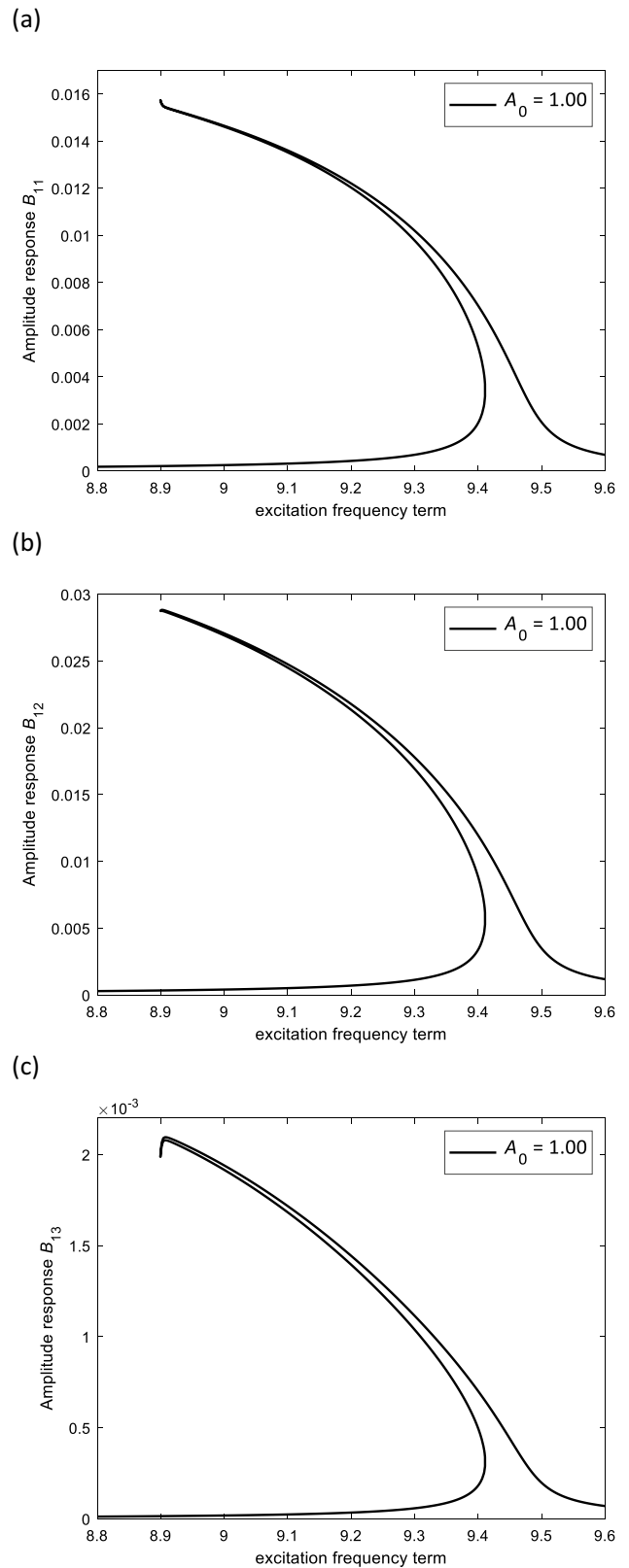


**Fig. 10** Axial amplitude-frequency response of geometrically imperfect ( $A_0=1.0$ ) AFG CNT strengthened porous beam (uniform open-cell porosity with  $\alpha_1=0.4$ ) **a** first coordinate, **b** second coordinate, and **c** third coordinate

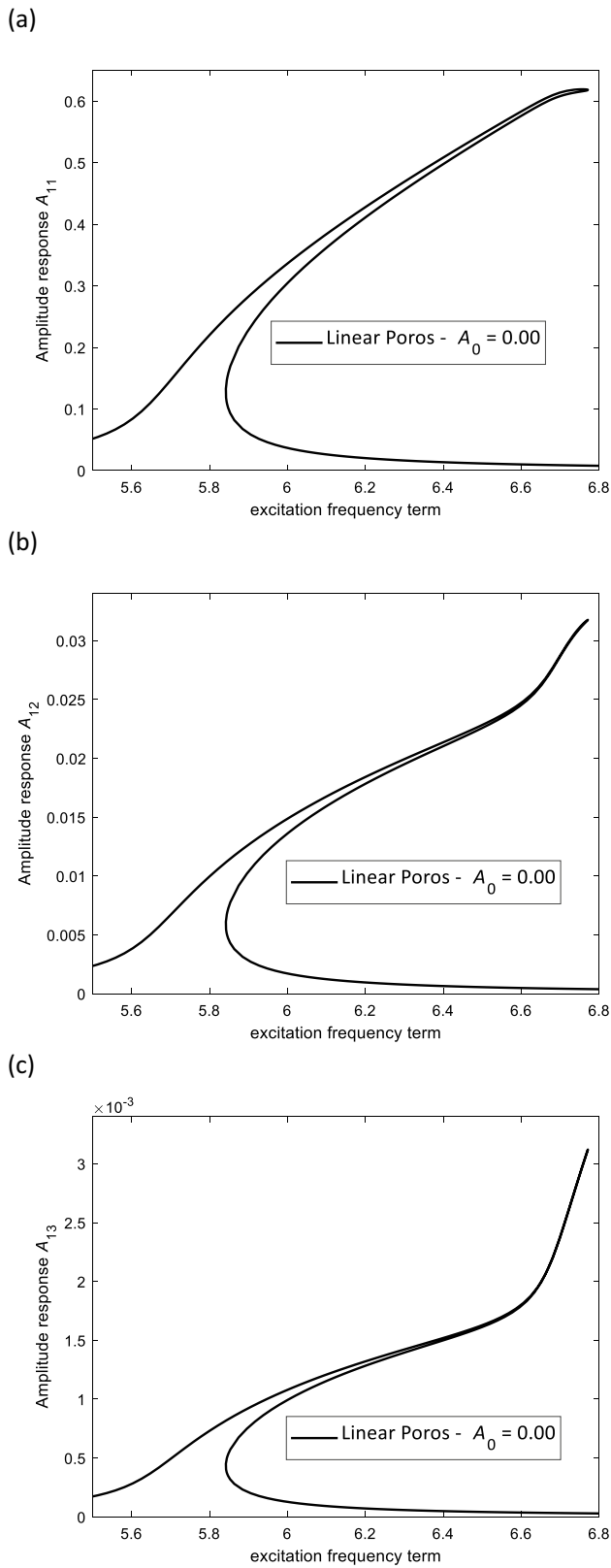


**Fig. 11** Transverse amplitude-frequency response of geometrically perfect AFG CNT strengthened porous beam (linear closed-cell porosity with  $\alpha_1=0.4$ ) **a** first coordinate, **b** second coordinate, and **c** third coordinate

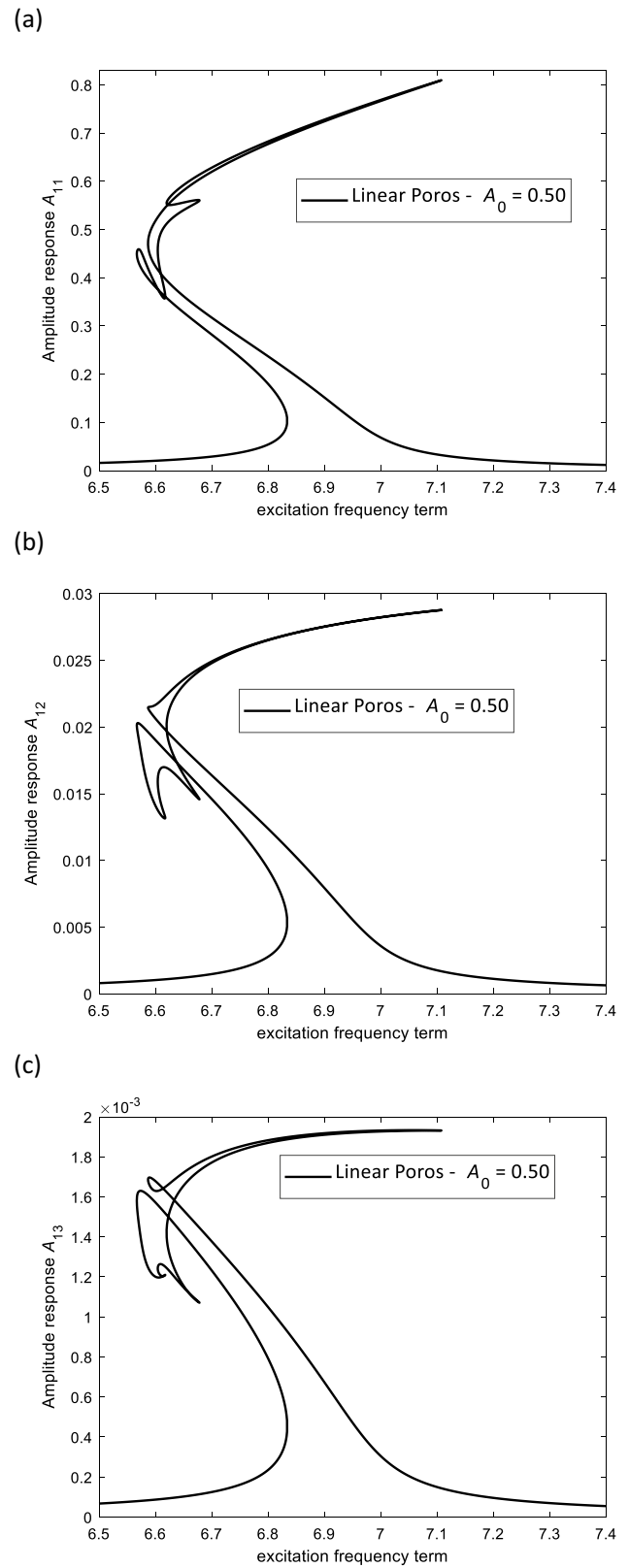


**Fig. 12** Transverse amplitude-frequency response of geometrically imperfect ( $A_0=0.5$ ) AFG CNT strengthened porous beam (linear closed-cell porosity with  $\alpha_1=0.4$ ) **a** first coordinate, **b** second coordinate, and **c** third coordinate

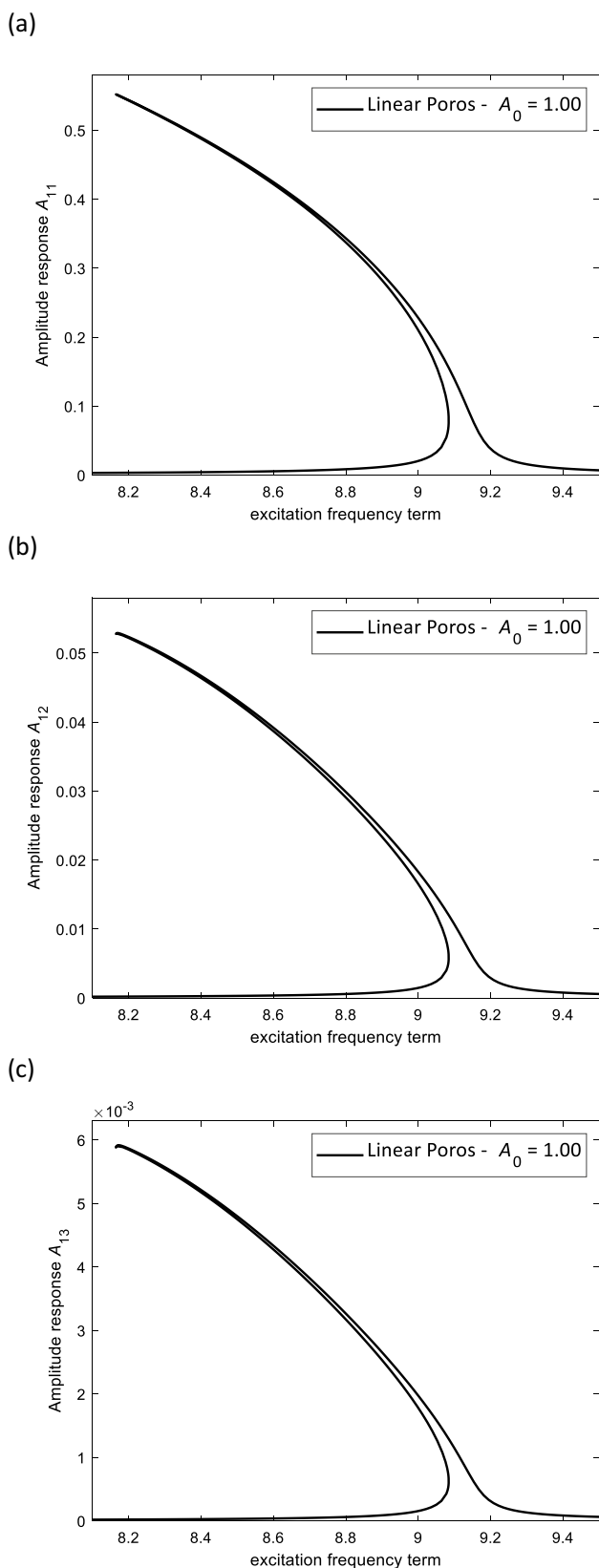


**Fig. 13** Transverse amplitude-frequency response of geometrically imperfect ( $A_0=1.0$ ) AFG CNT strengthened porous beam (linear closed-cell porosity with  $\alpha_1=0.4$ ) **a** first coordinate, **b** second coordinate, and **c** third coordinate

and the differential of Eq. (29) is written as

$$\frac{dR}{d\Omega} = -\left(\frac{\partial G(R, \Omega)}{\partial R}\right)^{-1} \left(\frac{\partial G(R, \Omega)}{\partial \Omega}\right). \tag{30}$$

By putting frequency parameter as the input, the amplitudes of the equations of motion are obtained. It should be mentioned that this sequential method fails when the singularity is obtained at  $\partial G(R, \Omega)/\partial R$  (at the turning point) [38]. Accordingly, a continuation term ( $\alpha_{arc}$ ) should be added to the system and parameters  $R$  and  $\Omega$  are defined as a function of this parameter as [39]

$$R = R(\alpha_{arc}), \quad \Omega = \Omega(\alpha_{arc}), \tag{31}$$

where Eq. (30) is rewritten by the definition given in Eq. (31) as [38]

$$\begin{aligned} &\left(\frac{\partial G(R, \Omega)}{\partial R}\right) \frac{dR}{d\alpha_{arc}} + \left(\frac{\partial G(R, \Omega)}{\partial \Omega}\right) \frac{d\Omega}{d\alpha_{arc}} \\ &= \begin{bmatrix} \frac{\partial G(R, \Omega)}{\partial R} & \frac{\partial G(R, \Omega)}{\partial \Omega} \end{bmatrix} \begin{Bmatrix} \frac{dR}{d\alpha_{arc}} \\ \frac{d\Omega}{d\alpha_{arc}} \end{Bmatrix} = 0. \end{aligned} \tag{32}$$

The tangent vector  $\begin{Bmatrix} \frac{dR}{d\alpha_{arc}} \\ \frac{d\Omega}{d\alpha_{arc}} \end{Bmatrix}$  has unit length with normal-

ising  $\alpha_{arc}$  as [40]

$$\begin{aligned} &\left(\frac{d\Omega}{d\alpha_{arc}}\right)^2 + \left(\frac{dR_1}{d\alpha_{arc}}\right)^2 + \dots + \left(\frac{dR_N}{d\alpha_{arc}}\right)^2 \\ &+ \dots + \left(\frac{dR_{2N-1}}{d\alpha_{arc}}\right)^2 + \left(\frac{dR_{2N}}{d\alpha_{arc}}\right)^2 = 1. \end{aligned} \tag{33}$$

Accordingly, an additional equation for updating  $\alpha_{arc}$  along with  $R$  and omega is written using Eq. (33) as

$$\begin{aligned} &-(\alpha_{arc} - \alpha_{arc}^{old})^2 + (R_1 - R_1^{old})^2 + \dots + (R_N - R_N^{old})^2 + \\ &\dots + (R_{2N-1} - R_{2N-1}^{old})^2 + (R_{2N} - R_{2N}^{old})^2 = \Theta(R, \Omega, \alpha_{arc}) = 0. \end{aligned} \tag{34}$$

The iteration process starts from an initial guess which in this study, the initial guess is made by solving the linear part of Eq. (29). Equations (32) and (34) are solved simultaneously using the initial guess and the process is repeated to reach a converged result. Then the frequency is evolved by [41]

$$\Omega_{new} = \Omega_{old} + \Delta\Omega, \tag{35}$$

and also, the dynamic equilibrium coefficients by

$$A_{mn} = A_{mn} + \Delta A_{mn}, \tag{36}$$

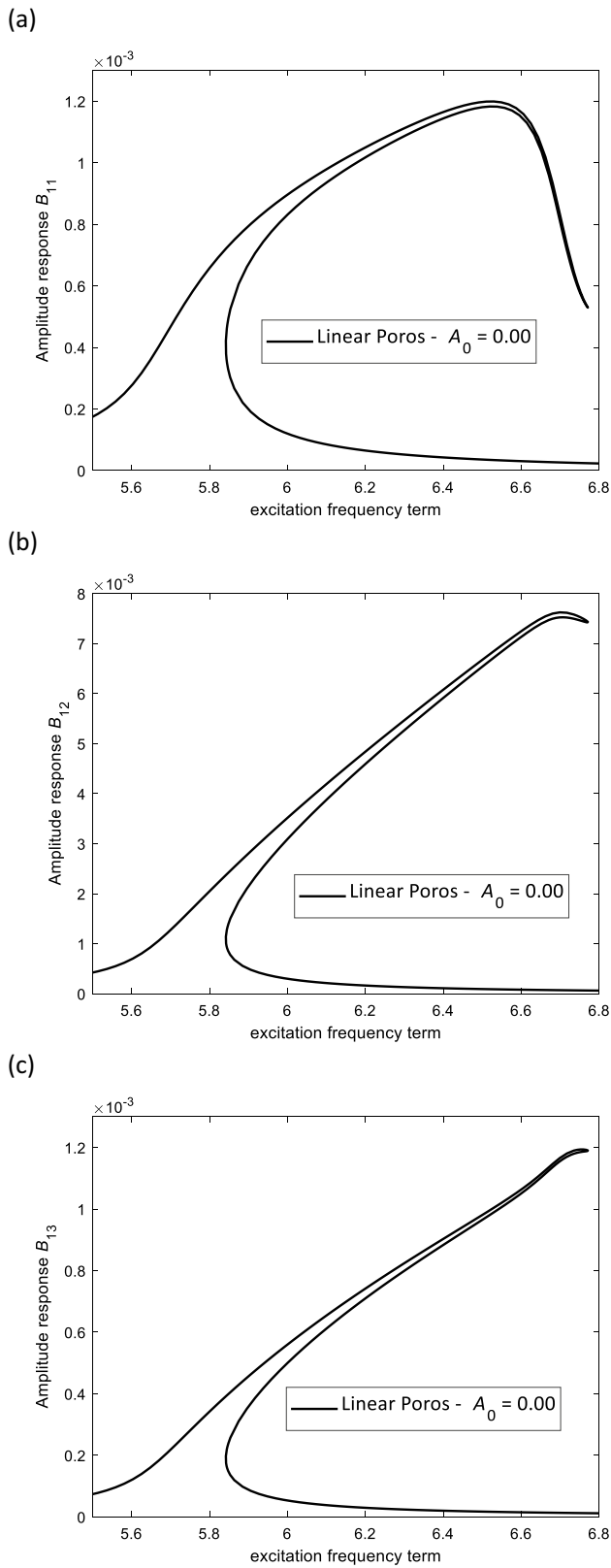


**Fig. 14** Axial amplitude-frequency response of geometrically perfect AFG CNT strengthened porous beam (linear closed-cell porosity with  $\alpha_1=0.4$ ) **a** first coordinate, **b** second coordinate, and **c** third coordinate

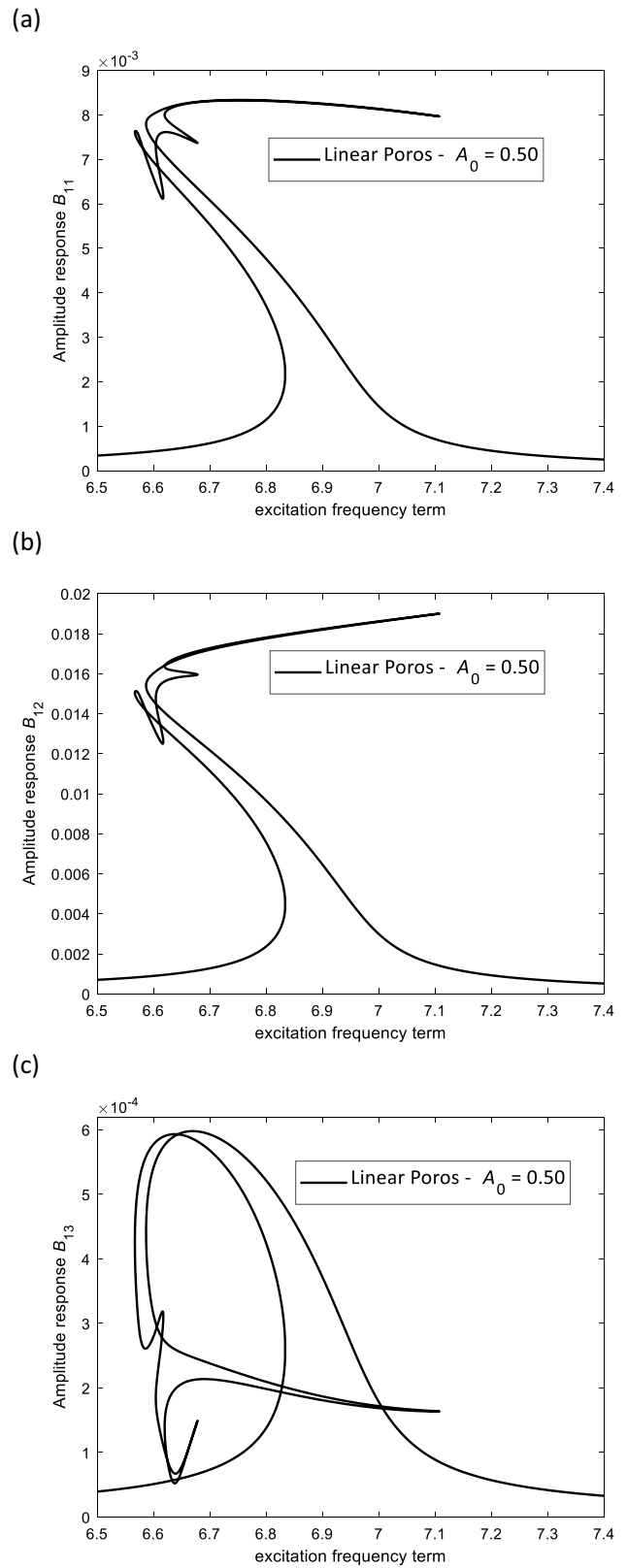


**Fig. 15** Axial amplitude-frequency response of geometrically imperfect ( $A_0=0.5$ ) AFG CNT strengthened porous beam (linear closed-cell porosity with  $\alpha_1=0.4$ ) **a** first coordinate, **b** second coordinate, and **c** third coordinate



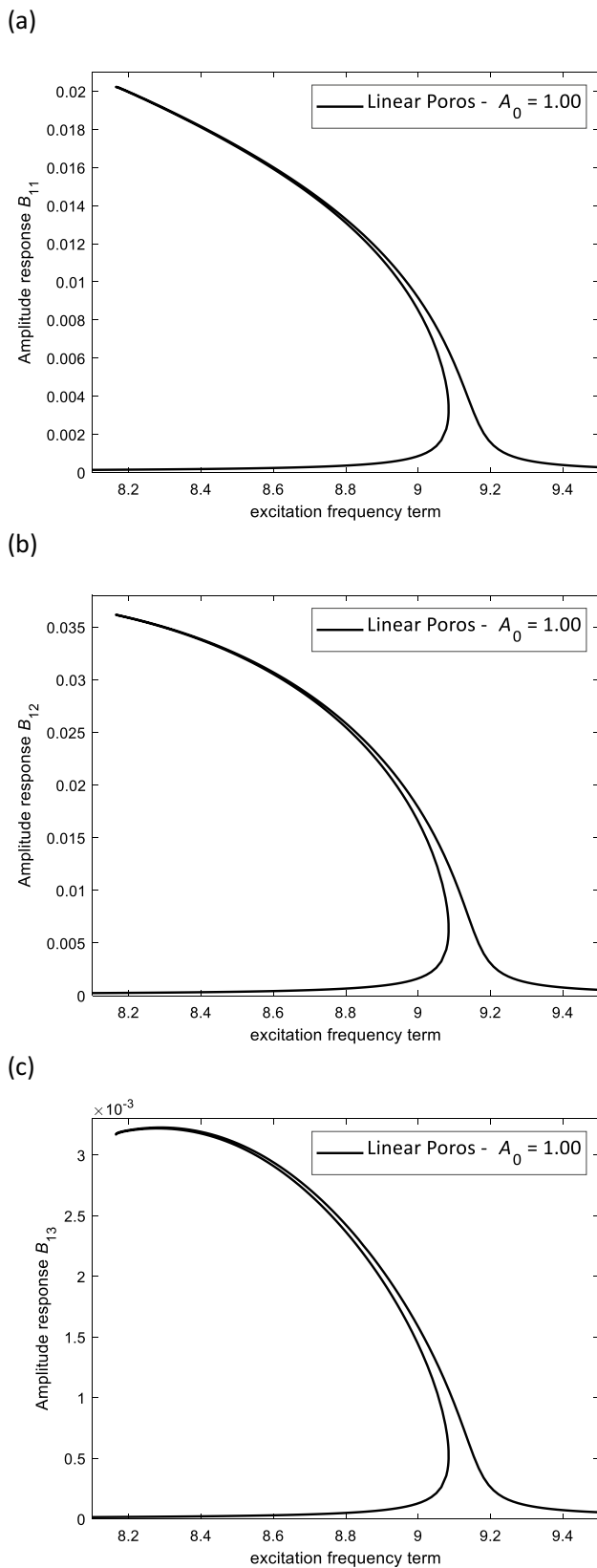


**Fig. 16** Axial amplitude-frequency response of geometrically imperfect ( $A_0=1.0$ ) AFG CNT strengthened porous beam (linear closed-cell porosity with  $\alpha_1=0.4$ ) **a** first coordinate, **b** second coordinate, and **c** third coordinate

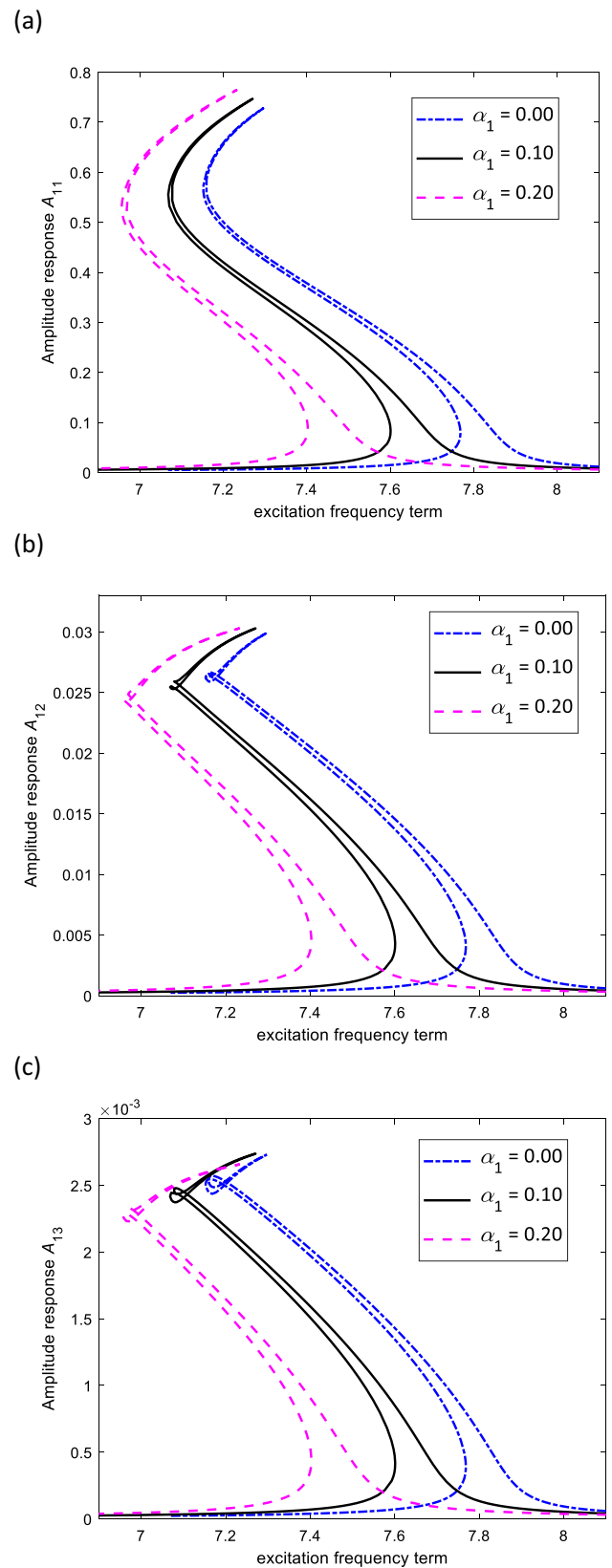


**Fig. 17** Influence of porosity on the transverse amplitude-frequency response of geometrically imperfect AFG CNT strengthened porous beam—linear porous closed-cell model **a**  $\alpha_1=0.00$ , **b**  $\alpha_1=0.10$ , and **c**  $\alpha_1=0.20$

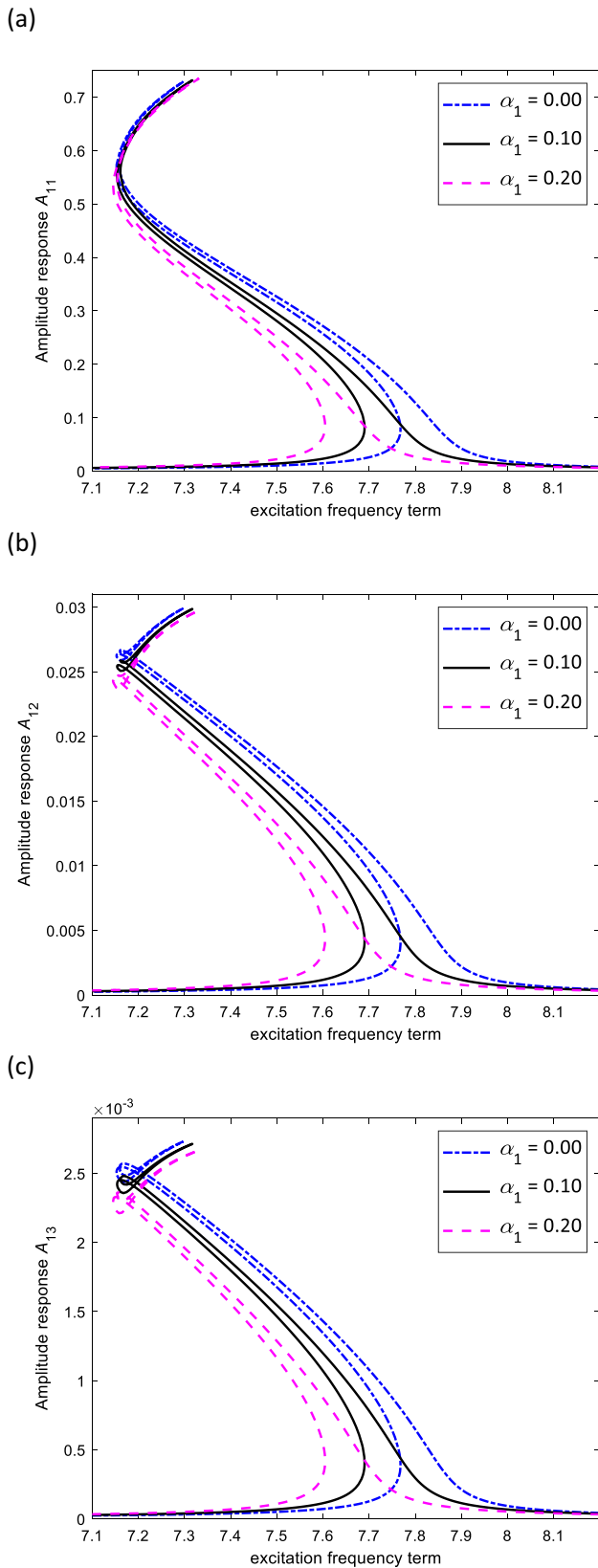


**Fig. 18** Influence of porosity on the *transverse* amplitude-frequency response of geometrically imperfect AFG CNT strengthened porous beam—*un-symmetric porous closed-cell model* **a**  $\alpha_1=0.00$ , **b**  $\alpha_1=0.10$ , and **c**  $\alpha_1=0.20$

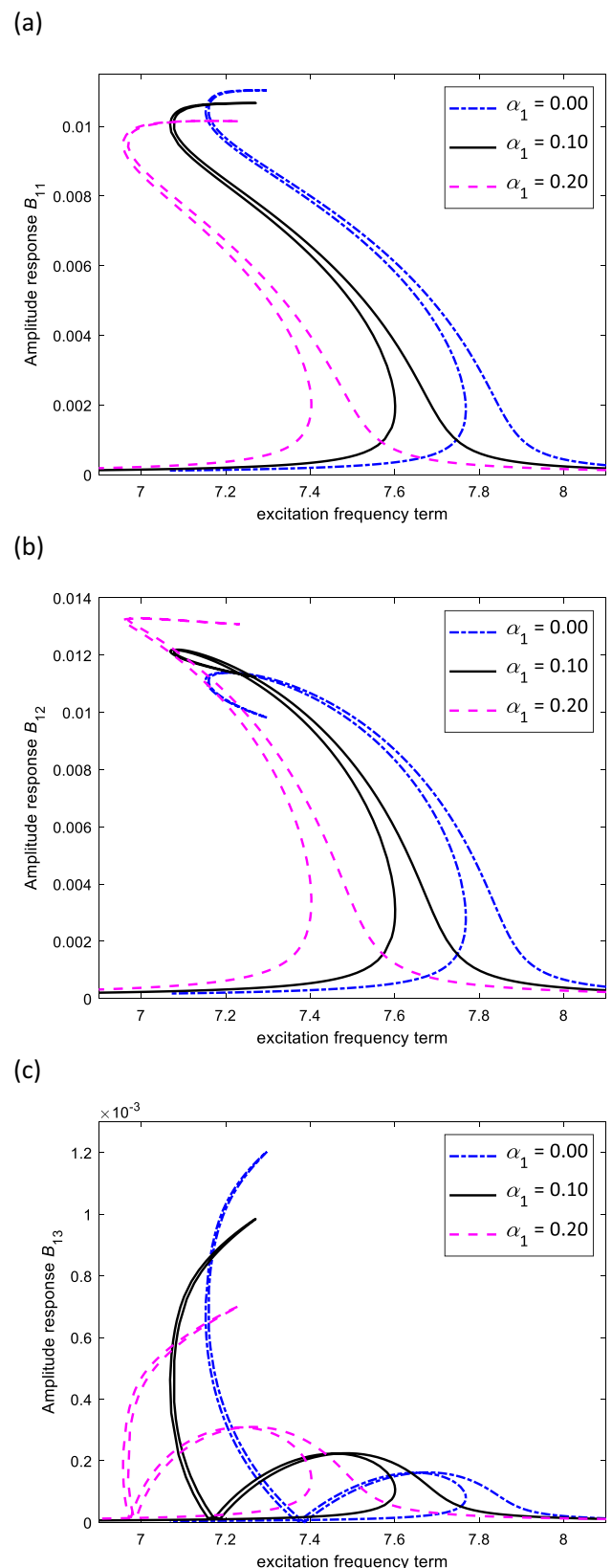


**Fig. 19** Influence of porosity on the *axial* amplitude-frequency response of geometrically imperfect AFG CNT strengthened porous beam—*linear porous closed-cell model* **a**  $\alpha_1=0.00$ , **b**  $\alpha_1=0.10$ , and **c**  $\alpha_1=0.20$

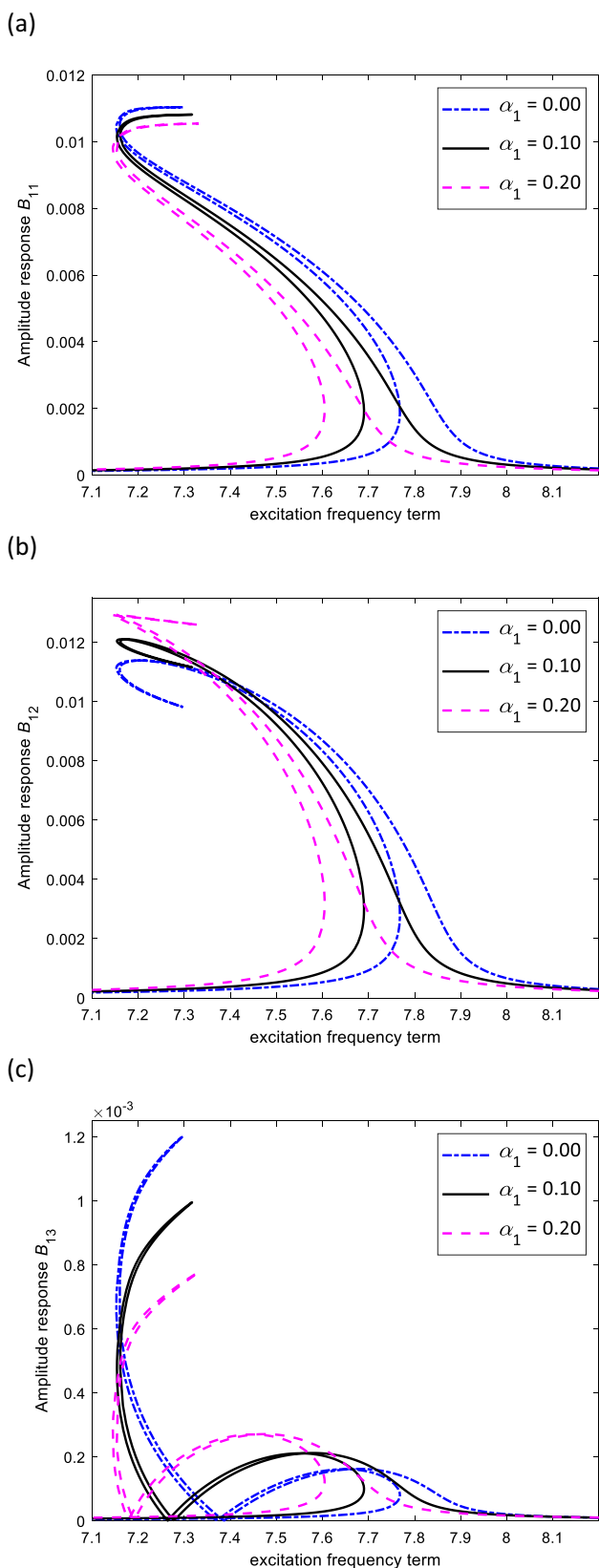


**Fig. 20** Influence of porosity on the axial amplitude-frequency response of geometrically imperfect AFG CNT strengthened porous beam—*un-symmetric porous closed-cell model* **a**  $\alpha_1=0.00$ , **b**  $\alpha_1=0.10$ , and **c**  $\alpha_1=0.20$

$$B_{mn} = B_{mn} + \Delta B_{mn}, \tag{37}$$

and the process is repeated.

### 3 CNT fibre effect on nonlinear coupled response

For AFG CNT strengthened imperfect beams, the equations of motion and solution procedure to obtain the nonlinear dynamic response are presented in the previous section. In this section, by defining the problem with the geometrical and physical properties as in Ref. [36]  $b=0.2$  m,  $h=0.1$  m,  $L=2$  m,  $E_m = 2.5$  GPa,  $E_{CNT}=5646.6$  GPa,  $\rho_m = 1190$  kg/m<sup>3</sup>,  $\rho_{CNT}=1400$  kg/m<sup>3</sup>,  $k=1$ ,  $V_{CNT,total}=5\%$  and  $V_{CNT,left}=2.5\%$ ,  $e_1=0.14$ ,  $\nu=0.3$  and non-dimensional external force as  $F=5$  with a modal damping 0.075, the influence of various parameters on the nonlinear forced vibration behaviour of the system with pinned- pinned boundary conditions is discussed.

One of the main analysis of this paper is to examine the effect of adding CNT fibres to imperfect beam models and show the impact on the nonlinear response. In the previous study [36], the improvements in the linear response of the system has been investigated and here, the nonlinear frequency response will be presented to clarify the nonlinear response of the system to the presence of an external harmonic load.

To this end, firstly, the influence of AFG varying the CNT volume fraction is analysed for a beam with symmetric porous closed cell as [42, 43]

$$\text{Symmetric} \rightarrow \begin{cases} \alpha_1(x) = \alpha_{10} \cos\left(\frac{\pi x}{a}\right) \\ \alpha_2(x) = \alpha_{20} \cos\left(\frac{\pi x}{a}\right) \end{cases}, \tag{38}$$

$$\begin{aligned} \text{Closed-cell cellular} &\rightarrow \alpha_{20} \\ &= 1.121 \left(\frac{\alpha_1(x_i)}{\alpha_{10}}\right)^{-1} \left[-\sqrt[2.3]{1 - \alpha_1(x_i)} + 1\right]. \end{aligned} \tag{39}$$

with  $\alpha_{10}=0.2$ , geometry imperfection  $A_0=0.5$  and mass imperfection of  $M=5$  at  $x_0=0.3$ . For this imperfect beam model, CNT distribution is assumed as  $V_{cnt,Total}=5\%$  linear variation through the length with  $V_{cnt,Left}=[1\%, 2\%, 3\%]$ . Results for transverse dynamic equilibrium coordinates can be seen in Fig. 2 with respect to non-dimensional frequency parameter ( $\Omega^{0.5}$ ) showing that increasing the CNT distribution variation has a substantial effect in varying the amplitude response of the system and increasing the  $V_{CNT,Left}$  for this beam model sweeps the excitation frequency to the right side. Besides, it can be seen that increasing the  $V_{CNT,Left}$

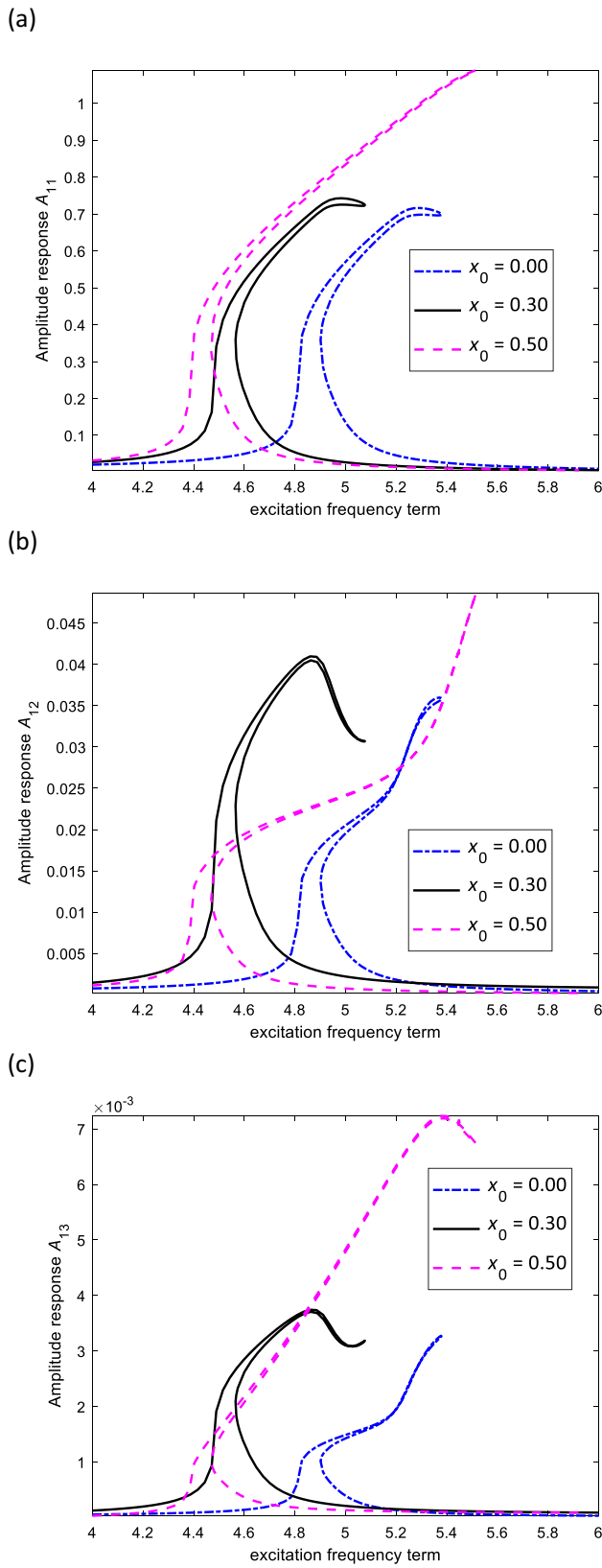


**Fig. 21** Influence of the mass imperfection position on the *transverse* amplitude-frequency response of imperfect AFG CNT strengthened porous beam **a**  $x_0=0.00$ , **b**  $x_0=0.30$ , and **c**  $x_0=0.50$

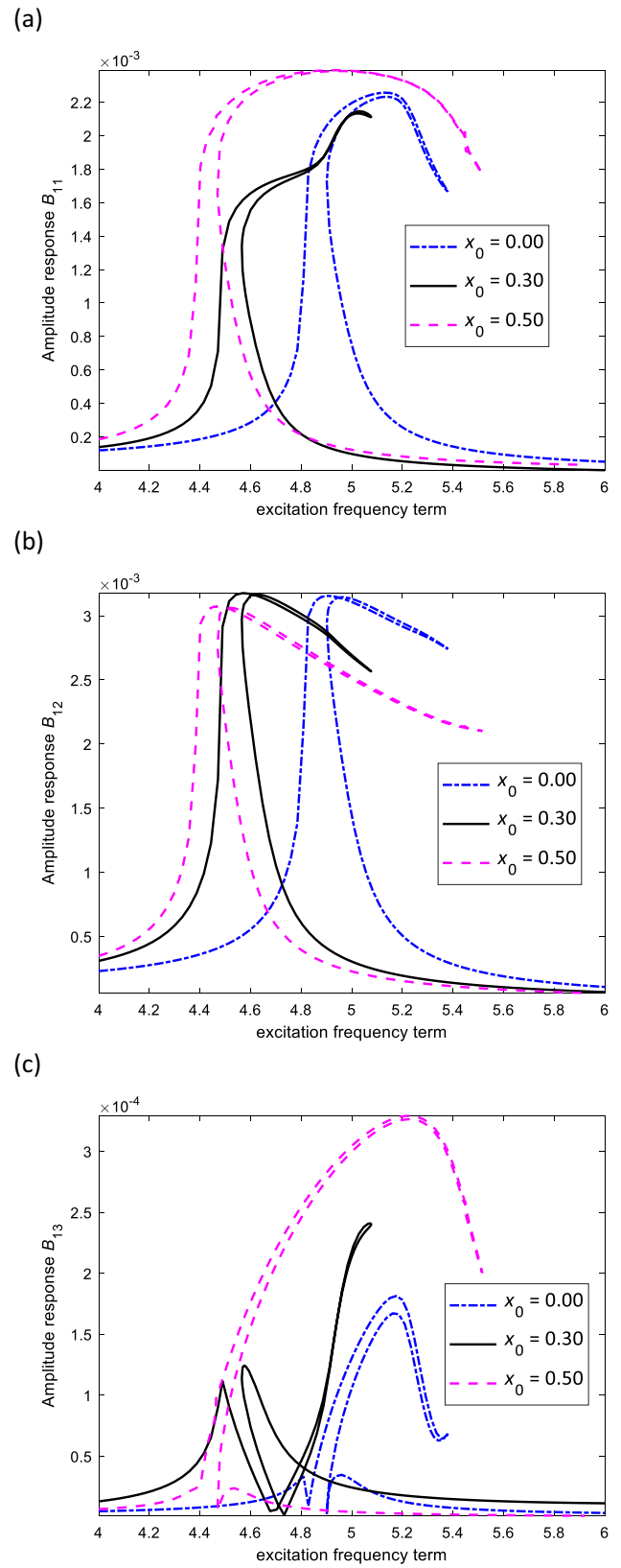


**Fig. 22** Influence of the mass imperfection position on the *axial* amplitude-frequency response of imperfect AFG CNT strengthened porous beam **a**  $x_0=0.00$ , **b**  $x_0=0.30$ , and **c**  $x_0=0.50$

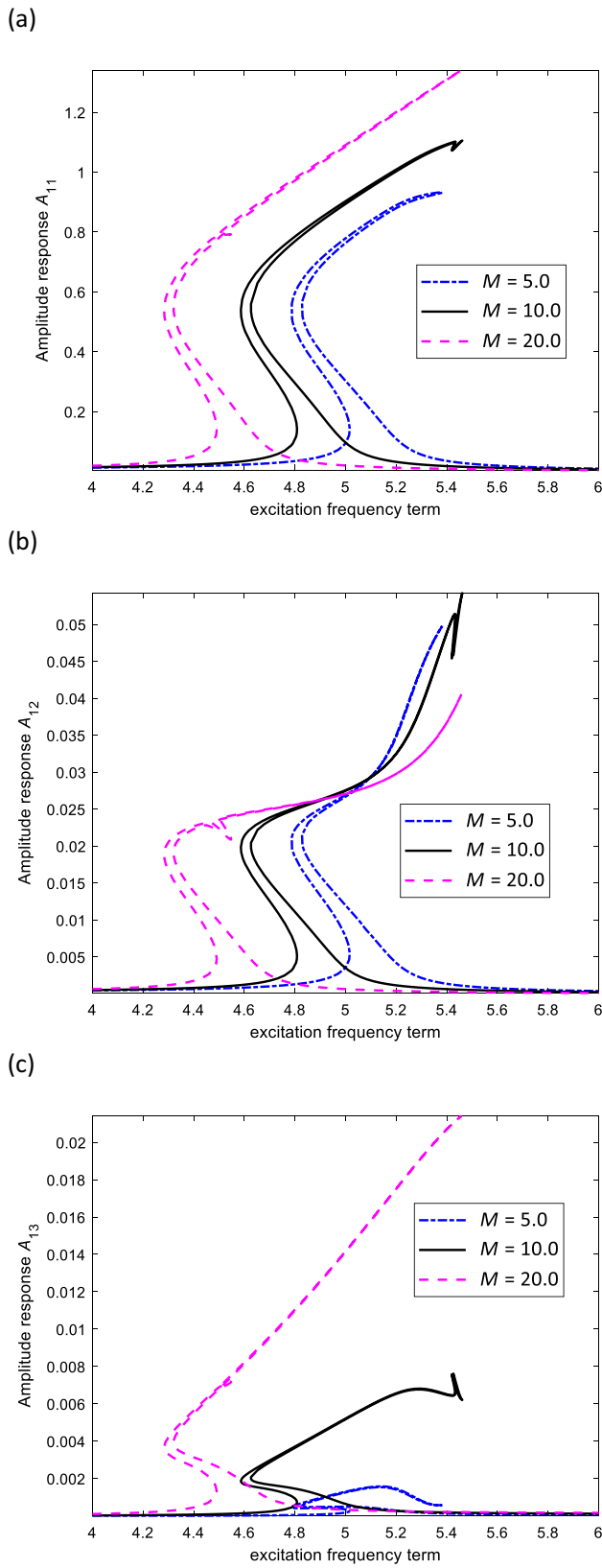


**Fig. 23** Influence of the mass imperfection on the *transverse* amplitude-frequency response of imperfect AFG CNT strengthened porous beam **a**  $M=5$ , **b**  $M=10$ , and **c**  $M=20$

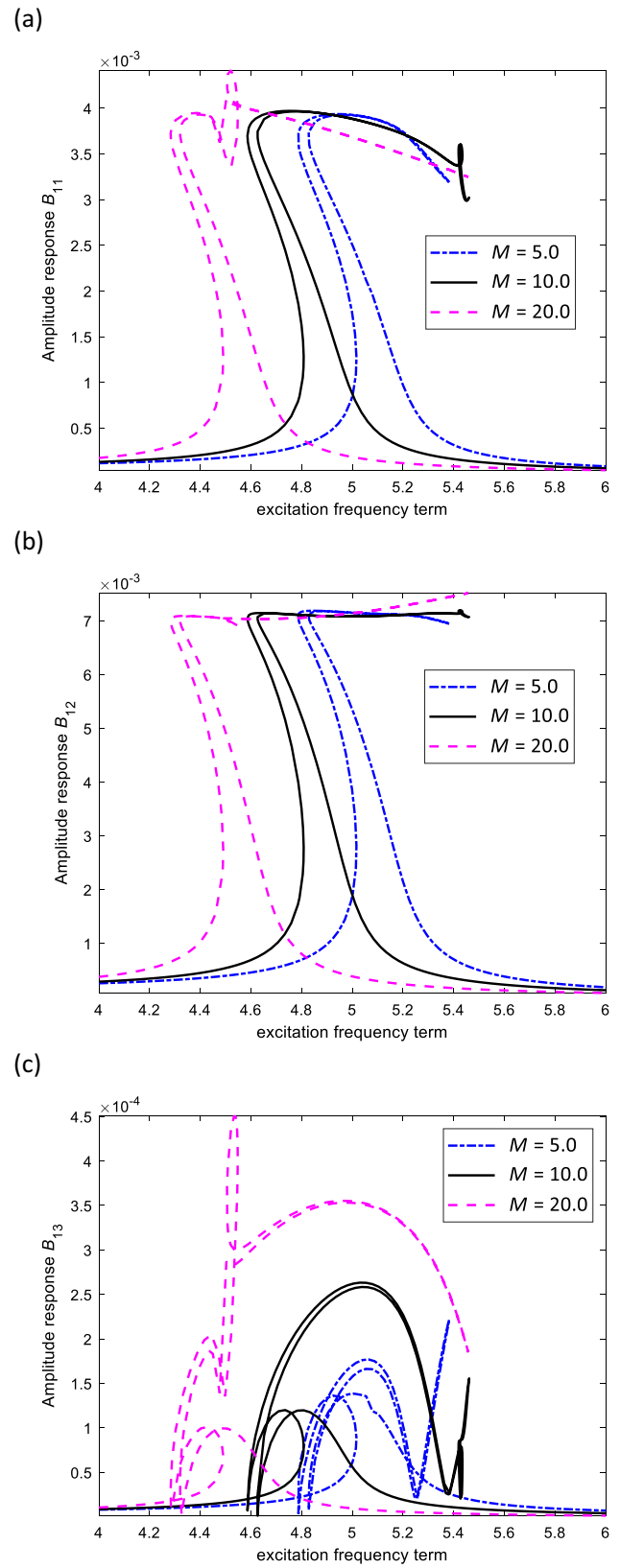


**Fig. 24** Influence of the mass imperfection on the *axial* amplitude-frequency response of imperfect AFG CNT strengthened porous beam **a**  $M=5$ , **b**  $M=10$ , and **c**  $M=20$

from 1 to 3% leads to lower coupling between the transverse modes by increasing the maximum amplitude of the first generalised coordinate and decreasing it for the other two coordinates.

Frequency amplitude responses for axial dynamic equilibrium coordinates are shown in Fig. 3 which in contrast to the transverse response, increasing the CNT volume fraction in the left side of the beam from 1 to 3% decreases the peak of the first axial coordinate and increases the peak of the second coordinate. Besides, increasing the CNT volume fraction for this beam model sweeps the excitation frequency to the right side.

Moreover, the influence of the  $V_{cnt,Total}$  inside the matrix is analysed by considering uniform CNT distribution in the beam and varying the CNT volume fraction as  $V_{cnt,Total} = [1\%, 2\%, 3\%]$ . Figure 4 shows the influence of the CNT fibres on the transverse vibration response of the imperfect beam model showing that the frequency response of the system sweeps to the right side for all the coordinates by increasing the fibre volume fraction. The maximum amplitude of the first transverse coordinate does not change by this variation but the second and third transverse coordinates lose amplitude.

For the axial motion, the influence of the CNT fibres volume fraction is shown in Fig. 5 indicating that increasing  $V_{cnt,Total}$  from 1 to 3 percent leads to lower amplitude response for the first and third coordinates while not changing it for the second coordinate. The frequency response of the system sweeps to the right side for all the coordinates by increasing  $V_{cnt,Total}$ .

#### 4 Geometrical imperfection effect on nonlinear coupled response

In this section, by defining the problem with the geometrical and physical properties as previous section, the influence of the geometrical imperfection on the nonlinear forced vibration response of the system with simply-supported boundary conditions is discussed. For the case of having a beam with uniform porosity of  $\alpha_{10} = 0.4$  with open-cell model as [43, 44]

$$\text{Uniform} \rightarrow \begin{cases} \alpha_1 = \alpha_{10} \\ \alpha_2 = \alpha_{20} \end{cases}, \tag{40}$$

$$\text{Open-cell solids} \rightarrow \alpha_{20} = -\sqrt{1 - \alpha_{10}} + 1, \tag{41}$$

without the mass imperfection, the frequency response of the beam is presented in Fig. 6 for the first three transverse dynamic coordinates of a geometrically perfect beam model with respect to non-dimensional excitation frequency parameter, and in Figs. 7 and 8 for having geometrical imperfection as  $A_0 = 0.5$  and  $A_0 = 1$ , respectively. It can be seen that by adding the geometrical imperfection to the system, the stiffness hardening behaviours of geometrically perfect beam model changes to stiffness softening for the given properties.

Moreover, the max amplitude of the first generalised coordinate increases first by adding geometrical imperfection as  $A_0 = 0.5$  but decreases after increasing the imperfection to  $A_0 = 1$ . However, the second generalised transverse coordinate's maximum amplitude increases by increasing the geometrical imperfection indicating a higher coupling between modes by having this type of imperfection.

For the axial motion, by considering the geometrical imperfection as  $A_0 = 0.5$  and  $A_0 = 1$ , the coupling between the equations of motion leads to nonlinear frequency response in axial direction which is shown in Figs. 9 and 10 for  $A_0 = 0.5$  and  $A_0 = 1$ , respectively. For the case of axial dynamic equilibrium coordinates, increasing the geometrical imperfection from 0.5 to 1 leads to higher maximum amplitudes for all the first three axial coordinates.

Moreover, for the case of having linear porosity of  $\alpha_{10} = 0.4$  for closed-cell model as [36]

$$\text{Linear} \rightarrow \begin{cases} \alpha_1(x) = \alpha_{10}(1 + x) \\ \alpha_2(x) = \alpha_{20}(1 + x) \end{cases}, \tag{42}$$

in contrast to the uniform porous model, the coupling between the axial and transverse geometrically perfect frequency responses exist due to un-symmetric porosity through the thickness. Figures 11, 12, 13 show the first three transverse dynamic coordinates of linear porous beam model having  $A_0 = 0, 0.5$  and  $1$ , respectively. It can be seen that for this type of porosity, increasing the geometrical imperfection to  $A_0 = 0.5$  and  $A_0 = 1.0$  leads to significant change in the frequency response from hardening to softening behaviour with more complicated responses compared to the uniform porosity model; however, the maximum amplitude response follows the same variation as uniform porous model.

For the axial coordinates in the linear porous model, frequency-amplitude responses are shown in Figs. 14, 15, 16 for  $A_0 = 0, 0.5$  and  $1$ , respectively. It can be seen that the first dynamic equilibrium axial coordinate has higher maximum amplitude in uniform model compared to the linear model for  $A_0 = 0.5$  while this is opposite for  $A_0 = 1$ . Besides, for both linear and uniform porous models, considering the geometrical imperfection sweeps the frequency response peak to higher excitation frequencies.

## 5 Porosity imperfection effect on nonlinear coupled response

For the given properties at Sect. 3, the influence of imperfection porosity type on the nonlinear frequency response of the system is analysed in this section. To this end, for linear porous closed-cell model, the porosity parameter is varied as  $\alpha_{10} = [0.0, 0.1, 0.2]$  by having geometrical imperfection of  $A_0 = 0.5$  and the transverse frequency response coordinates are shown in Fig. 17. Similarly, for non-symmetric closed-cell porous model as [36]

$$\text{Non-symmetric} \rightarrow \begin{cases} \alpha_1(x) = \alpha_{10} \cos\left(\frac{\pi x}{a} - \frac{\pi}{4}\right) \\ \alpha_2(x) = \alpha_{20} \cos\left(\frac{\pi x}{a} - \frac{\pi}{4}\right) \end{cases}, \quad (43)$$

the same analysis it done and the results are shown in Fig. 18 for the transverse frequency responses; it can be seen that for transverse motion, the maximum amplitude-frequency response coordinates do not change significantly in magnitude for the non-symmetric model. For the linear porous model, increasing the porosity term from 0 to 0.2 slightly increases the peak of the amplitude response for the first transverse coordinate. Besides, the frequency response of the beam model sweeps to left by increasing the porosity parameter.

For the axial motion, increasing the porosity term from 0 to 0.2 leads to higher coupling between the first two axial coordinates in both the linear (Fig. 19) and un-symmetric (Fig. 20) porous models by decreasing the max value for the amplitude of the first axial coordinate and increasing the amplitude of the second one. The third coordinate loses amplitude in both porous models by increasing the porosity of the system. Similar to the transverse coordinates, the frequency response of the beam model sweeps to left by increasing the porosity parameter and the porosity effect in non-symmetric closed-cell porous model is considerably lower than the linear porous closed-cell model.

## 6 Mass imperfection effect on nonlinear coupled response

Another important imperfection in manufacturing and operating CNT strengthened beams is mass imperfection. In this section, the influence of having mass imperfection and its position on the nonlinear dynamic response of the system is shown.

### 6.1 Mass imperfection position effect

For the case of having a beam with symmetric porous  $\alpha_{10} = 0.2$  closed-cell model, geometrical imperfection  $A_0 = 0.3$  and mass imperfection of  $M = 10$  is considered; the rest of the properties are as defined at Sect. 3. For this CNT strengthened beam model, the influence of the position of the mass imperfection is analysed by having  $x_0 = [0.0, 0.3, 0.5]$  and shown in Fig. 21 for transverse dynamic equilibrium coordinates; it can be seen that the position of the mass imperfection has a significant effect in varying the nonlinear frequency response in which for  $x_0 = 0.5$ , the amplitudes of all the first three coordinates increase significantly.

For the axial motion, the dynamic equilibrium coordinates are shown in Fig. 22 by having  $x_0 = [0.0, 0.3, 0.5]$ ; it can be seen that moving the position of the mass imperfection from 0 to 0.5 increases the amplitudes of the first and third axial coordinates but decreases the amplitude of the second coordinate. It should also be mentioned that increasing the position of the mass imperfection from 0 to 0.5 sweeps the frequency response of the beam model to the left side.

### 6.2 Mass imperfection weight effect

The influence of the mass imperfection weight is analysed by having CNT strengthened beam model with non-symmetric closed-cell porosity with  $\alpha_{10} = 0.3$ , geometry imperfection  $A_0 = 0.5$  and the mass imperfection position 0.5. Results are shown in Fig. 23 for transverse dynamic equilibrium coordinates; it can be seen that increasing the mass imperfection weight sweeps the curves to the left side and increases the peak and nonlinearity in the first and third coordinates of the transverse response.

Similarly, for the axial motion, the results for axial coordinates are shown in Fig. 24 indicating that all the three axial coordinates show higher peak of amplitude by increasing the weight of the mass imperfection.

## 7 Conclusions

A comprehensive analysis on the nonlinear dynamics of imperfect beams strengthened with CNT fibres was presented in this study for the first time by grading the CNTs through the length of the beam. The beam was assumed with geometrical and mass imperfection together with porosity imperfection. The geometrical imperfection was presented by assuming a slight curve in the beam and the porosity was assumed to vary through the thickness of the beam. The porosity was modelled by assuming open cell, closed cell and simple form of the formulation, and the variation through the thickness was presented using a uniform,



un-symmetric, symmetric and linear variations. The coupled axial and transverse equations of motion were presented. They show nonlinear coupling due to porosity, imperfections and large deformations. The equations of motion were solved using a combination of the Galerkin scheme and a dynamic equilibrium technique. By examining the nonlinear dynamic behaviour of the system, the following outcomes were obtained:

- For the studied case, geometric imperfection has a significant effect in varying the nonlinear behaviour from hardening to softening.
- For the symmetric beam, the axial/transverse coupling is insignificant while for an un-symmetric beam, the axial/transverse coupling is relevant and both the axial and transverse coordinates show rich nonlinear dynamics.
- The type of the porosity and its variation has a direct effect in the nonlinear response of the system for both the axial and transverse coordinates.
- The system shows high sensitivity to the mass imperfection and its position. Increasing the mass weight and moving it to the middle of the beam shifts the resonance towards smaller frequency.
- It is shown that the CNTs have a significant effect on the nonlinear response of imperfect beams and decrease the max value for the amplitude of the first coordinate of both axial and transverse motions.
- The distribution of the CNTs have also been examined. An increase of the nonuniformity of CNT grading shifts the resonance towards larger frequency.

Imperfection in the system lead to complicated nonlinear frequency response. This shows the importance of considering these imperfections to accurately model the beam structure. This investigation can be extended to different types of fibre-reinforced structures.

### Appendix A

For a hollow beam model, by having a geometrical imperfection and neglecting the shear deformation, the nonzero stress-deformation and strain-deformation terms are written as [36]

$$\epsilon_{xx} = \frac{\partial u(x, t)}{\partial x} - z \frac{\partial^2 w(x, t)}{\partial x^2} + \frac{1}{2} \left( \frac{\partial w(x, t)}{\partial x} \right)^2 + \frac{\partial w(x, t)}{\partial x} \frac{dw_0(x)}{dx}, \tag{A1}$$

$$\sigma_{xx} = \frac{E(x, z)}{1 - \nu^2(x, z)} \left[ \frac{\partial u(x, t)}{\partial x} + \frac{1}{2} \left( \frac{\partial w(x, t)}{\partial x} \right)^2 - z \frac{\partial^2 w(x, t)}{\partial x^2} + \frac{\partial w(x, t)}{\partial x} \frac{dw_0(x)}{dx} \right], \tag{A2}$$

where  $E$  is the Young’s modulus,  $\nu$  is the Poisson ratio,  $w$  and  $u$  are the transverse and axial displacements in  $z$  and  $x$  directions and  $w_0$  is the geometrical imperfection. It is assumed that the Young’s modulus and the Poisson ratio vary as a function of the position  $(x, z)$  within the beam, as a consequence of the porosity and the functionally graded distribution of the CNT along the length. Since the CNT volume fraction varies along the length and the porosity varies along the thickness of the beam, the Young’s modulus and density are defined as [35]

$$\begin{aligned} \left\{ \begin{matrix} E(x, z) \\ \rho(x, z) \end{matrix} \right\} &= \left\{ \begin{matrix} E_m \\ \rho_m \end{matrix} \right\} - \left[ \left\{ \begin{matrix} E_m \\ \rho_m \end{matrix} \right\} V_m(x) \right. \\ &\quad \left. + \left\{ \begin{matrix} e_1 E_{CNT} \\ \rho_{CNT} \end{matrix} \right\} V_{CNT}(x) \right] \left\{ \begin{matrix} \alpha_1(z) \\ \alpha_2(z) \end{matrix} \right\} \\ &\quad + \left( \left\{ \begin{matrix} e_1 E_{CNT} \\ \rho_{CNT} \end{matrix} \right\} - \left\{ \begin{matrix} E_m \\ \rho_m \end{matrix} \right\} \right) V_{CNT}(x), \end{aligned} \tag{A3}$$

where subscripts  $m$  and  $CNT$  denote the matrix and CNT properties,  $V$  is the volume fraction and  $e_1$  is the effective coefficient indicating the efficiency of CNTs in strengthening the Young’s modulus of the composite. Parameters  $\alpha_1$  and  $\alpha_2$  are the porosity terms affecting the Young’s modulus and density terms respectively with porosity coefficients  $\alpha_{10}$  and  $\alpha_{20}$  which for closed-cell cellular models, open-cell solids and simplified models are related together by [42, 43]

$$\alpha_{20} = \begin{cases} \frac{1.121 \left( 1 - \sqrt[3]{1 - \alpha_1(z)} \right)}{\left( \frac{\alpha_1(z)}{\alpha_{10}} \right)} \rightarrow \text{(Closed-cell cellular)} \\ 1 - \sqrt{1 - \alpha_{10}} \rightarrow \text{(Open-cell solids)} \\ \alpha_{10} \rightarrow \text{(Simplified models)} \end{cases}, \tag{A4}$$



where  $\alpha_1$  and  $\alpha_2$  can vary in the thickness direction following a specific function which will be discussed further. Besides, the CNT volume fraction varies through the length as [36]

$$\begin{cases} V_m(x) = 1 - V_{CNT}(x), \\ V_{CNT}(x) = V_{CNT-L} \left(1 - \frac{x}{L}\right)^k + V_{CNT-R} \left[1 - \left(1 - \frac{x}{L}\right)^k\right], \end{cases} \quad 0 \leq x \leq L, \quad (\text{A5})$$

where the subscripts  $R$  and  $L$  denote the right and left ends of the beam and  $k$  is the variation power term. The potential and kinetic energy terms are written as [36]

$$U = \frac{1}{2} \int_0^L \int_A \frac{E(x, z)}{1 - \nu^2(x)} \left[ \frac{\partial u(x, t)}{\partial x} - z \frac{\partial^2 w(x, t)}{\partial x^2} + \frac{1}{2} \left( \frac{\partial w(x, t)}{\partial x} \right)^2 + \left( \frac{\partial w(x, t)}{\partial x} \right) \left( \frac{dw_0(x)}{dx} \right) \right]^2 dAdx, \quad (\text{A6})$$

$$\begin{aligned} K = \frac{1}{2} M \int_0^L & \left[ \left( \frac{\partial w(x, t)}{\partial t} \right)^2 + \left( \frac{\partial u(x, t)}{\partial t} \right)^2 \right] \delta_d(x - x_0) \\ & + \frac{1}{2} \int_0^L \int_A \rho(x, z) \left[ \left( \frac{\partial u(x, t)}{\partial t} - z \frac{\partial^2 w(x, t)}{\partial x \partial t} \right)^2 + \left( \frac{\partial w(x, t)}{\partial t} \right)^2 \right] dAdx. \end{aligned} \quad (\text{A7})$$

In Eq. (A7),  $\delta_d$  is the Dirac delta function,  $M$  represents the lumped mass imperfection, and  $x_0$  is the axial position of  $M$ .

## References

- Edwards K (1998) An overview of the technology of fibre-reinforced plastics for design purposes. *Mater Des* 19:1–10
- Bajracharya RM, Manalo AC, Karunasena W, Lau K-T (1980–2015) An overview of mechanical properties and durability of glass-fibre reinforced recycled mixed plastic waste composites. *Mater Des* 62(2014):98–112
- Vermeeren C (2003) An historic overview of the development of fibre metal laminates. *Appl Compos Mater* 10:189–205
- Reid SR, Zhou G (2000) Impact behaviour of fibre-reinforced composite materials and structures. Elsevier, Amsterdam
- Pimenta S, Pinho ST (2011) Recycling carbon fibre reinforced polymers for structural applications: technology review and market outlook. *Waste Manage* 31:378–392
- Tebeta R, Fattahi A, Ahmed N (2020) Experimental and numerical study on HDPE/SWCNT nanocomposite elastic properties considering the processing techniques effect. *Microsyst Technol*. <https://doi.org/10.1007/s00542-020-04784-y>
- Yourdkhani M, Liu W, Baril-Gosselin S, Robitaille F, Hubert P (2018) Carbon nanotube-reinforced carbon fibre-epoxy composites manufactured by resin film infusion. *Compos Sci Technol* 166:169–175
- Gojny F, Wichmann M, Köpke U, Fiedler B, Schulte K (2004) Carbon nanotube-reinforced epoxy-composites: enhanced stiffness and fracture toughness at low nanotube content. *Compos Sci Technol* 64:2363–2371
- Boncel S, Sundaram RM, Windle AH, Kozioł KK (2011) Enhancement of the mechanical properties of directly spun CNT fibers by chemical treatment. *ACS Nano* 5:9339–9344
- Sobolkin A, Mechtcherine V, Khavrus V, Maier D, Mende M, Ritschel M, Leonhardt A (2012) Dispersion of carbon nanotubes and its influence on the mechanical properties of the cement matrix. *Cement Concr Compos* 34:1104–1113
- Fattahi A, Safaei B, Qin Z, Chu F (2021) Experimental studies on elastic properties of high density polyethylene-multi walled carbon nanotube nanocomposites. *Steel Compos Struct* 38:177
- Sahmani S, Fattahi A (2018) Development of efficient size-dependent plate models for axial buckling of single-layered graphene nanosheets using molecular dynamics simulation. *Microsyst Technol* 24:1265–1277
- Tran V-K, Pham Q-H, Nguyen-Thoi T (2020) A finite element formulation using four-unknown incorporating nonlocal theory for bending and free vibration analysis of functionally graded nanoplates resting on elastic medium foundations. *Eng Comput*. <https://doi.org/10.1007/s00366-020-01107-7>
- Yang X, Sahmani S, Safaei B (2020) Postbuckling analysis of hydrostatic pressurized FGM microsized shells including strain gradient and stress-driven nonlocal effects. *Eng Comput*. <https://doi.org/10.1007/s00366-019-00901-2>
- Fattahi A, Sahmani S, Ahmed N (2019) Nonlocal strain gradient beam model for nonlinear secondary resonance analysis of functionally graded porous micro/nano-beams under periodic hard excitations. *Mech Based Des Struct Mach*. <https://doi.org/10.1080/15397734.2019.1624176>

16. Sahmani S, Fattahi A, Ahmed N (2019) Size-dependent nonlinear forced oscillation of self-assembled nanotubes based on the nonlocal strain gradient beam model. *J Braz Soc Mech Sci Eng* 41:1–16
17. Lu P, Lee H, Lu C, Zhang P (2007) Application of nonlocal beam models for carbon nanotubes. *Int J Solids Struct* 44:5289–5300
18. Reddy J, Pang S (2008) Nonlocal continuum theories of beams for the analysis of carbon nanotubes. *J Appl Phys* 103:023511
19. Sahmani S, Fattahi AM, Ahmed N (2019) Analytical mathematical solution for vibrational response of postbuckled laminated FG-GPLRC nonlocal strain gradient micro-/nanobeams. *Eng Comput* 35:1173–1189
20. Wang Q (2005) Wave propagation in carbon nanotubes via nonlocal continuum mechanics. *J Appl Phys* 98:124301
21. Peddieson J, Buchanan GR, McNitt RP (2003) Application of nonlocal continuum models to nanotechnology. *Int J Eng Sci* 41:305–312
22. Wu Q, Chen H, Gao W (2019) Nonlocal strain gradient forced vibrations of FG-GPLRC nanocomposite microbeams. *Eng Comput*. <https://doi.org/10.1007/s00366-019-00794-1>
23. Sahmani S, Fattahi AM, Ahmed N (2020) Develop a refined truncated cubic lattice structure for nonlinear large-amplitude vibrations of micro/nano-beams made of nanoporous materials. *Eng Comput* 36:359–375
24. Fattahi A, Mondali M (2014) Theoretical study of stress transfer in platelet reinforced composites. *J Theor Appl Mech* 52:3–14
25. Al-Furjan M, Habibi M, Ni J, Won Jung D, Tounsi A (2020) Frequency simulation of viscoelastic multi-phase reinforced fully symmetric systems. *Eng Comput*. <https://doi.org/10.1007/s00366-020-01200-x>
26. Shi Z, Yao X, Pang F, Wang Q (2017) An exact solution for the free-vibration analysis of functionally graded carbon-nanotube-reinforced composite beams with arbitrary boundary conditions. *Sci Rep* 7:12909
27. Joshi UA, Sharma SC, Harsha S (2011) Influence of dispersion and alignment of nanotubes on the strength and elasticity of carbon nanotubes reinforced composites. *J Nanotechnol Eng Med* 2:041007
28. Ke L-L, Yang J, Kitipornchai S (2010) Nonlinear free vibration of functionally graded carbon nanotube-reinforced composite beams. *Compos Struct* 92:676–683
29. Pourasghar A, Chen Z (2019) Effect of hyperbolic heat conduction on the linear and nonlinear vibration of CNT reinforced size-dependent functionally graded microbeams. *Int J Eng Sci* 137:57–72
30. Wu H, Yang J, Kitipornchai S (2016) Nonlinear vibration of functionally graded carbon nanotube-reinforced composite beams with geometric imperfections. *Compos B Eng* 90:86–96
31. Ke L-L, Yang J, Kitipornchai S (2013) Dynamic stability of functionally graded carbon nanotube-reinforced composite beams. *Mech Adv Mater Struct* 20:28–37
32. Fattahi A, Safaei B (2017) Buckling analysis of CNT-reinforced beams with arbitrary boundary conditions. *Microsyst Technol* 23:5079–5091
33. Civalek Ö, Avcar M (2020) Free vibration and buckling analyses of CNT reinforced laminated non-rectangular plates by discrete singular convolution method. *Eng Comput*. <https://doi.org/10.1007/s00366-020-01168-8>
34. Mahesh V, Harursampath D (2020) Nonlinear vibration of functionally graded magneto-electro-elastic higher order plates reinforced by CNTs using FEM. *Eng Comput*. <https://doi.org/10.1007/s00366-020-01098-5>
35. Khaniki HB, Ghayesh MH (2020) On the dynamics of axially functionally graded CNT strengthened deformable beams. *Eur Phys J Plus* 135:415
36. Khaniki HB, Ghayesh MH, Hussain S, Amabili M (2020) Porosity, mass and geometric imperfection sensitivity in coupled vibration characteristics of CNT-strengthened beams with different boundary conditions. *Eng Comput*. <https://doi.org/10.1007/s00366-020-01208-3>
37. Sundararajan P, Noah S (1997) Dynamics of forced nonlinear systems using shooting/arc-length continuation method—application to rotor systems. *J Vib Acoust*. <https://doi.org/10.1115/1.2889694>
38. Nayfeh AH, Balachandran B (2008) Applied nonlinear dynamics: analytical, computational, and experimental methods. Wiley, Hoboken
39. Von Groll G, Ewins DJ (2001) The harmonic balance method with arc-length continuation in rotor/stator contact problems. *J Sound Vib* 241:223–233
40. Chan TF, Keller H (1982) Arc-length continuation and multigrid techniques for nonlinear elliptic eigenvalue problems. *SIAM J Sci Stat Comput* 3:173–194
41. Dickson K, Kelley C, Ipsen IC, Kevrekidis IG (2007) Condition estimates for pseudo-arclength continuation. *SIAM J Numer Anal* 45:263–276
42. Roberts AP, Garboczi EJ (2001) Elastic moduli of model random three-dimensional closed-cell cellular solids. *Acta Mater* 49:189–197
43. Gibson I, Ashby MF (1982) The mechanics of three-dimensional cellular materials. *Proc R Soc Lond A Math Phys Sci* 382:43–59
44. Gao K, Li R, Yang J (2019) Dynamic characteristics of functionally graded porous beams with interval material properties. *Eng Struct* 197:109441

**Publisher's Note** Springer Nature remains neutral with regard to jurisdictional claims in published maps and institutional affiliations.